X Chromosome Domain Architecture Regulates Caenorhabditis elegans Lifespan but Not Dosage Compensation

Article *in* Developmental Cell · October 2019

DOI: 10.1016/j.devcel.2019.08.004

CITATION
1

READS
58

11 authors, including:

Phillip Andrew Frankino
University of California, Berkeley
30 PUBLICATIONS **27** CITATIONS

SEE PROFILE

Qian Bian
University of California, Berkeley
18 PUBLICATIONS **659** CITATIONS

SEE PROFILE

Katie Podshivalova
The Scripps Research Institute
17 PUBLICATIONS **246** CITATIONS

SEE PROFILE

Article

Developmental Cell

X Chromosome Domain Architecture Regulates *Caenorhabditis elegans* Lifespan but Not Dosage Compensation

Graphical Abstract

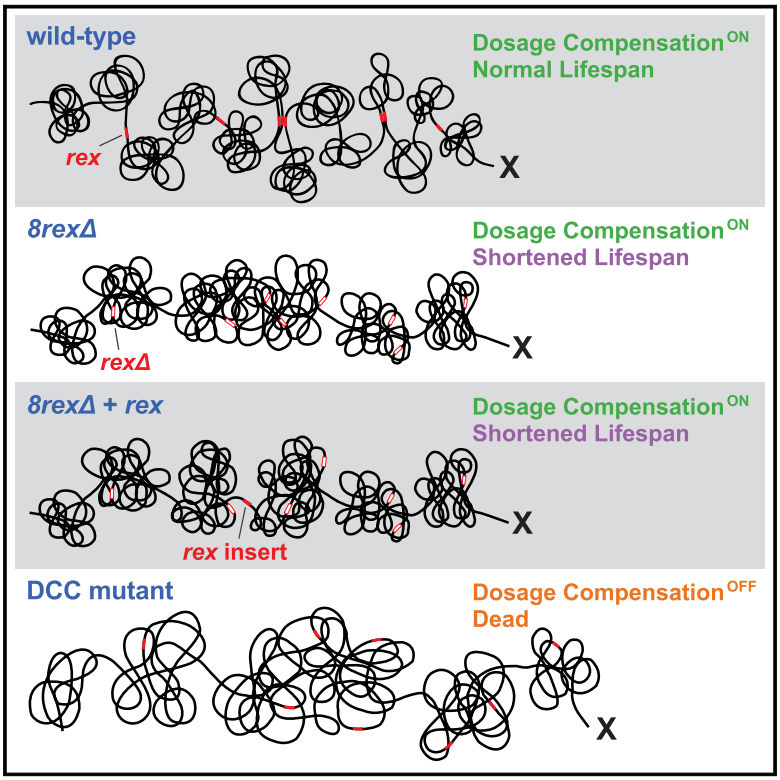

Highlights

- A DCC recruitment site (*rex*) is necessary and sufficient to form a TAD boundary on X
- Destroying X TADs by deleting only 8 *rex* sites does not disrupt dosage compensation
- DCC establishes other X structures and promotes X compaction independently of TADs
- Destroying X TADs reduces thermotolerance, accelerates aging, and shortens lifespan

Authors

Erika C. Anderson, Phillip A. Frankino, Ryo Higuchi-Sanabria, ..., Cynthia Kenyon, Andrew Dillin, Barbara J. Meyer

Correspondence

bjmeyer@berkeley.edu

In Brief

Anderson et al. show that binding of the condensin dosage compensation complex (DCC) to individual high-affinity sites on nematode X chromosomes is necessary and sufficient to establish boundaries for topologically associating domains (TADs). Eliminating DCC-dependent domain architecture does not compromise dosage compensation but does reduce thermotolerance, accelerate aging, and shorten lifespan.

Anderson et al., 2019, Developmental Cell *51*, 1–16
October 21, 2019
https://doi.org/10.1016/j.devcel.2019.08.004

CellPress

Developmental Cell
Article

X Chromosome Domain Architecture Regulates *Caenorhabditis elegans* Lifespan but Not Dosage Compensation

Erika C. Anderson,[1] Phillip A. Frankino,[1,4] Ryo Higuchi-Sanabria,[1,4] Qiming Yang,[1] Qian Bian,[1,3] Katie Podshivalova,[2] Aram Shin,[1] Cynthia Kenyon,[2] Andrew Dillin,[1] and Barbara J. Meyer[1,5,*]
[1]Howard Hughes Medical Institute and Department of Molecular and Cell Biology, University of California, Berkeley, Berkeley, CA 94720, USA
[2]Calico Life Sciences, South San Francisco, CA 94080, USA
[3]Present address: Shanghai Institute of Precision Medicine, Ninth People's Hospital, Shanghai Jiao Tong University School of Medicine, Shanghai, China
[4]These authors contributed equally
[5]Lead Contact
*Correspondence: bjmeyer@berkeley.edu
https://doi.org/10.1016/j.devcel.2019.08.004

SUMMARY

Mechanisms establishing higher-order chromosome structures and their roles in gene regulation are elusive. We analyzed chromosome architecture during nematode X chromosome dosage compensation, which represses transcription via a dosage-compensation condensin complex (DCC) that binds hermaphrodite Xs and establishes megabase-sized topologically associating domains (TADs). We show that DCC binding at high-occupancy sites (*rex* sites) defines eight TAD boundaries. Single *rex* deletions disrupted boundaries, and single insertions created new boundaries, demonstrating that a *rex* site is necessary and sufficient to define DCC-dependent boundary locations. Deleting eight *rex* sites (*8rexΔ*) recapitulated TAD structure of DCC mutants, permitting analysis when chromosome-wide domain architecture was disrupted but most DCC binding remained. *8rexΔ* animals exhibited no changes in X expression and lacked dosage-compensation mutant phenotypes. Hence, TAD boundaries are neither the cause nor the consequence of DCC-mediated gene repression. Abrogating TAD structure did, however, reduce thermotolerance, accelerate aging, and shorten lifespan, implicating chromosome architecture in stress responses and aging.

INTRODUCTION

Interphase chromosomes are highly organized into a series of structures ranging from kilobase-scale chromatin loops to territories comprising hundreds of megabases (Gibcus and Dekker, 2013; Serizay and Ahringer, 2018; Yu and Ren, 2017). Dissecting the mechanisms underlying the formation of these interrelated structures and unraveling their functions require their precise manipulation, a task made challenging by the paucity of information about DNA sequences and factors required for higher-order chromosome organization.

We focus on topologically associating domains (TADs) of approximately 1 Mb that are characteristic of metazoan chromosomes. TADs were defined in mammalian cells as self-interacting domains (Dixon et al., 2012; Nora et al., 2012). Loci in one TAD interact predominantly with each other while being insulated from interactions with loci in neighboring TADs. Mechanisms that define TAD boundaries and the biological functions of TADs have been elusive. In mammalian cells, architectural proteins important for establishing TADs, such as the zinc-finger protein CTCF (CCCTC-binding factor) and the SMC complex cohesin, localize at boundaries between TADs (Dixon et al., 2012; Nora et al., 2012). The architectural proteins also play roles in essential cellular processes such as chromosome segregation (Hocquet et al., 2018; Morales and Losada, 2018), making the functional significance of TADs difficult to assess at the organismal level by depleting these proteins to disrupt TADs (Nora et al., 2017; Rao et al., 2017; Schwarzer et al., 2017). Rather than depleting multifunctional proteins, we eliminate TADs by deleting specific binding sites for an architectural protein complex and assess the effects on gene expression and animal development.

We analyzed chromosome architecture and its impact on gene expression in the context of *Caenorhabditis elegans* X chromosome dosage compensation, an essential process in which both gene expression and higher-order chromosome structure are regulated via a specialized condensin complex (Meyer, 2018). This dosage compensation complex (DCC) equalizes X expression between XO males and XX hermaphrodites by binding along both hermaphrodite X chromosomes and reducing transcription by half while also establishing an X structure composed of 1 Mb TADs (Crane et al., 2015). Without DCC binding, eight TAD boundaries are lost, causing X structure to resemble that of autosomes with fewer, less regularly spaced TAD boundaries. These remaining boundaries are DCC independent. All eight DCC-dependent TAD boundaries contain a high-affinity DCC binding site (*rex* site) (Crane et al., 2015), which typically includes multiple X-enriched motifs important for DCC binding (Albritton et al., 2017; Ercan et al., 2007; Jans et al., 2009; McDonel et al., 2006; Pferdehirt et al., 2011). The findings

that stable DCC binding near a gene is neither necessary nor sufficient for the dosage compensation of the gene and that transgenes integrated at multiple locations along X become compensated indicate that dosage compensation is a chromosome-wide process in which the DCC can act at a distance to repress transcription (Jans et al., 2009; Wheeler et al., 2016). Thus, DCC-dependent TAD structure could plausibly underlie the mechanism of gene repression.

In addition to condensin subunits, the DCC includes proteins important for loading of condensin onto X (SDC-2 and SDC-3) and a histone demethylase (DPY-21) responsible for enriching the histone modification H4K20me1 on X (Bian et al., 2018; Brejc et al., 2017). Loss of H4K20me1 enrichment causes partial disruption of dosage compensation, de-compaction of X, and weakening of DCC-dependent TAD boundaries (Brejc et al., 2017).

Mechanisms used by the DCC to remodel X chromosome topology and establish TADs are broadly relevant because condensin and other SMC complexes play key roles in shaping chromosome architecture in eukaryotes and prokaryotes. Condensin is essential for mitotic chromosome compaction and segregation in eukaryotes (Gibcus et al., 2018; Hirano, 2016), represses transcription in quiescent yeast (Swygert et al., 2019), and resolves newly replicated sister origins during DNA replication in *Bacillis subtilis* (Wang et al., 2017). Cohesin is required for the formation of most TAD boundaries in mammalian cells (Rao et al., 2017; Schwarzer et al., 2017).

The functions of TADs in gene regulation have not been well characterized. In principle, loss of TAD boundaries could be either a cause or consequence of transcriptional changes. In mammalian cells, disrupting a TAD boundary leads to merging of adjacent TADs, permitting enhancers to interact with additional genes and activate them ectopically. Developmental defects such as limb malformations can occur as a consequence (Franke et al., 2016; Lupiáñez et al., 2015; Narendra et al., 2015). In other contexts, transcription can control chromosome structure, as in *Caulobacter*, where transcription drives the formation of boundaries between chromosomal interaction domains (Le and Laub, 2016). Defining the relationship between TAD structure and gene regulation has been challenging because architectural proteins that establish TADs also bind and function at locations other than TAD boundaries, such as promoters, making it unclear whether the transcriptional changes resulting from their depletion are caused exclusively by altered TAD structure or by other roles of the proteins in gene regulation (Nora et al., 2017; Rao et al., 2017; Schwarzer et al., 2017).

Here, we defined the requirements for creating a DCC-dependent boundary by making a series of *rex* site deletions and insertions on X chromosomes and measuring the resulting chromosome structure. DCC binding at a high-occupancy *rex* site was necessary and sufficient to define the location of a boundary. By deleting all eight *rex* sites at the eight DCC-dependent boundaries, we eliminated DCC-dependent TAD structure and found that TADs do not drive dosage compensation. In the absence of TADs, the DCC promotes DNA interactions across X between loci within 0.1–1 Mb, which may underlie transcriptional repression. Although abrogating TAD structure in hermaphrodites by deleting *rex* sites did not disrupt dosage compensation, it did reduce thermotolerance, accelerate aging, and shorten lifespan, implicating higher-order chromosome structure in regulating stress responses and aging.

RESULTS

Deleting the Single *rex* Site at Each DCC-Dependent TAD Boundary Eliminated the Boundary

We dissected the mechanisms by which the DCC establishes TAD boundaries by analyzing the potential contributions of multiple factors. First, the presence of a high-occupancy *rex* site at each DCC-dependent boundary suggested that DCC binding at these strong *rex* sites might define the locations of boundaries. Second, DCC-mediated interactions between DCC-dependent boundaries are among the strongest long-range interactions on the X chromosome, suggesting that boundary formation might require not only DCC binding at *rex* sites, but also long-range interactions between *rex* sites located at DCC-dependent boundaries (Crane et al., 2015). Third, the DCC promotes interactions between *rex* sites within TADs (Crane et al., 2015), raising the possibility that these intra-TAD interactions might passively create boundaries by bringing loci together.

To assess the role in boundary formation of DCC binding at high-occupancy *rex* sites, we sequentially deleted the single *rex* site at each of the eight DCC-dependent TAD boundaries on X (Table S1) and measured the resulting chromosome structure (Figure 1A). Seven *rex* sites are in intergenic regions, and each *rex* deletion (400–1,100 bp) removed all motifs known to be important for DCC binding. The exception (*rex-33*) was deleted by removing the entire intron of the essential gene in which it resides. To verify that deletions eliminated DCC binding, we performed chromatin immunoprecipitation sequencing (ChIP-seq) using antibodies for the DCC-specific SMC protein DPY-27 and the non-condensin DCC subunit SDC-3, which helps load all condensin subunits onto X. Binding of both subunits was lost entirely at each deleted site, while DCC binding at dozens of remaining *rex* sites persisted (Figure S1A).

We examined the effects of *rex* deletions on chromosome structure by performing *in situ* genome-wide chromosome conformation capture studies(Hi-C) on wild-type embryos, a series of mutant embryos with increasing numbers of *rex* deletions, and DCC mutant embryos lacking DCC binding on X [*sdc-2(y93, RNAi)*] (Table S2). Previous fluorescence *in situ* hybridization experiments showed that deleting *rex-47* greatly diminished the associated TAD boundary (Crane et al., 2015). We confirmed this result by Hi-C. By comparing distance-normalized Hi-C interactions (Z-scores) between *rex-47Δ* and wild-type embryos, we found an increase in interactions across the deleted *rex* site (Figures 1B and S2A), verifying boundary loss. To quantify the extent of loss, we created X chromosome insulation profiles (Crane et al., 2015). Briefly, we calculated an insulation score for each locus by summing all interactions within a 500 kb window surrounding that locus. When comparatively few interactions occur across a locus, it has a low insulation score. Such a local minimum in the insulation profile is defined as a TAD boundary. *rex-47* is at a local minimum in the wild-type insulation profile, and the valley was eliminated in *rex-47Δ*, indicating complete loss of the TAD boundary (Figure 1B). Thus, the *rex* site defined the boundary location.

Next, we examined *3rexΔ* and *6rexΔ* chromosomes, in which additional *rex* sites were deleted from the center and right side

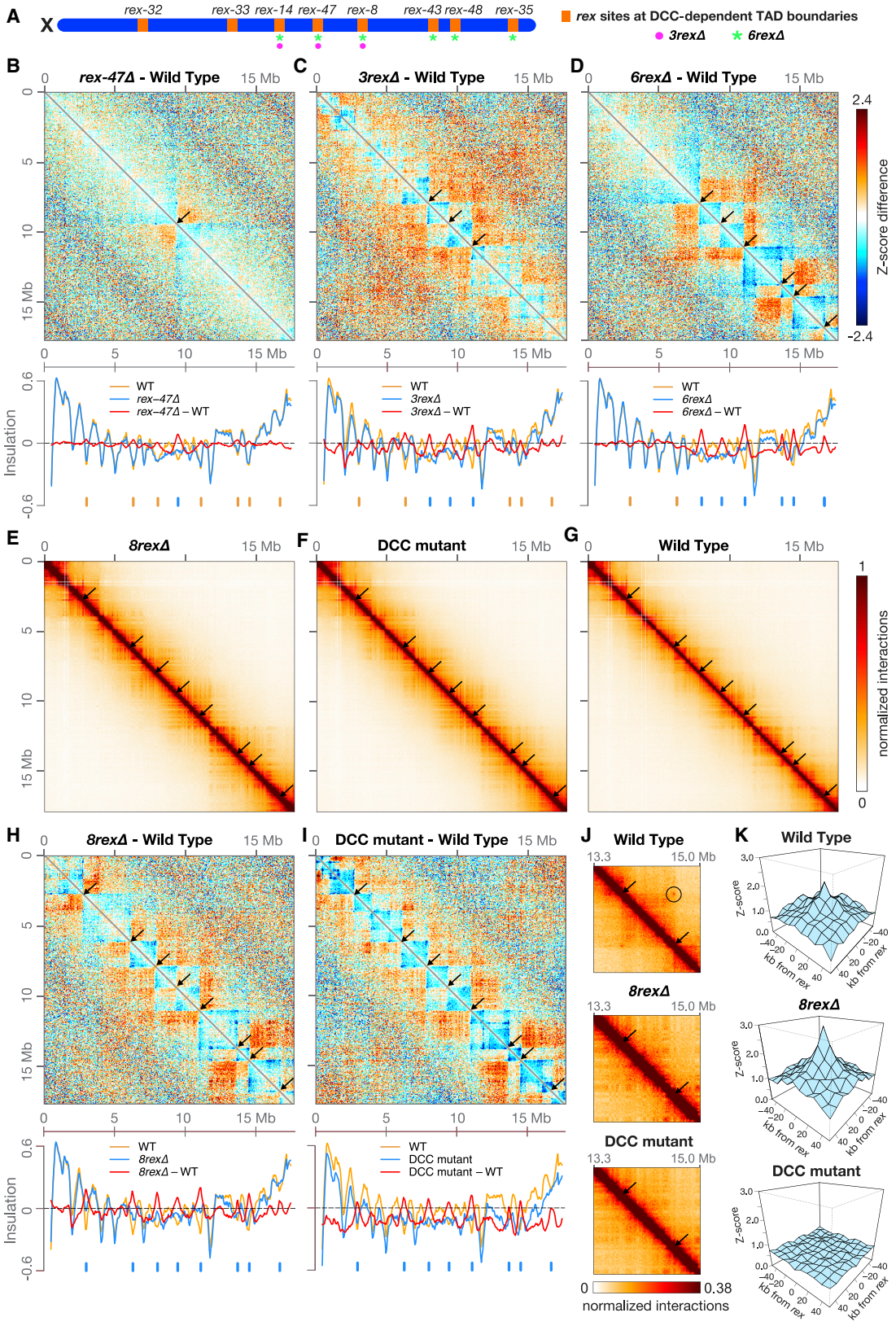

(legend on next page)

of X. The boundaries at the deleted *rex* sites were eliminated, but all other boundaries remained (Figures 1C, 1D, S2B, and S2C). No new boundaries emerged at the remaining weaker *rex* sites, indicating that high-occupancy *rex* sites do not impede lower-occupancy *rex* sites from forming boundaries.

Deleting all eight *rex* sites at the DCC-dependent boundaries recapitulated the disrupted TAD structure of X chromosomes in embryonic lethal DCC mutants that lack DCC binding. In both the *8rexΔ* and DCC mutants, seven TAD boundaries were eliminated, and the boundary at *rex-32* was dramatically weakened (Figures 1E–1J), while DCC-independent TAD boundaries on X and autosomes remained (Figures S2D–S2H). Although the DCC was bound to numerous *rex* sites across X in *8rexΔ* embryos (Figure S1A), removing only the eight *rex* sites at DCC-dependent TAD boundaries was sufficient to disrupt the TAD structure of X. Thus, a *rex* site is essential to define the location of each DCC-dependent TAD boundary.

Using *8rexΔ* embryos, we tested whether intra-TAD *rex-rex* interactions might passively create boundaries. We found that DCC-mediated interactions between the 22 highest-affinity non-boundary *rex* sites persisted in *8rexΔ* embryos (Figures 1K, S2I, and S2J), indicating that interactions between *rex* sites within the same TAD are not sufficient to create TAD boundaries on the native X. Instead, DCC binding to the eight *rex* sites at DCC-dependent TAD boundaries defines boundary location.

Inserting a Single High-Occupancy *rex* Site Created a New TAD Boundary on X, but Not on an Autosome

Having shown that a *rex* site is necessary to form a DCC-dependent TAD boundary, we asked whether a single *rex* site is sufficient to create a boundary. We inserted a high-occupancy *rex* site (*rex-32*) that forms a boundary at its endogenous location into a new location in the middle of the *8rexΔ* X chromosome (Figure 2A). The inserted *rex* site bound the DCC at a level comparable to that at its original location (Figure S4A), and it defined a new boundary of similar strength to the boundary at its endogenous site (Figures 2B, 2C, and 2F). Therefore, insertion of a single high-affinity DCC binding site is sufficient to create a TAD boundary on X. This boundary is the sole DCC-dependent boundary on the chromosome, revealing that boundary formation does not require interactions between DCC-dependent boundaries. However, we have not ruled out the possibility that interactions between the ectopic *rex* site and weaker, non-boundary *rex* sites may contribute to boundary formation.

A second *rex* site (*rex-8*) inserted 1.4 Mb downstream of the newly inserted *rex-32* site also defined a new TAD boundary (Figures 2D–2F). Boundary-to-boundary interactions occurred between the inserted *rex-8* and *rex-32* sites (Figure 2D, right), and the boundary at *rex-32* became slightly weaker (Figure 2F). Therefore, interactions between adjacent DCC-dependent boundaries do not strengthen boundaries.

To determine whether a *rex* site is sufficient to create a new boundary in the context of wild-type 3D architecture, we inserted *rex-32* into a new, non-boundary location on the right side of the wild-type X chromosome. Again, *rex-32* bound the DCC at a level similar to that at its endogenous location (Figure S4B) and defined a new boundary (Figures 2G and 2H). Thus, the native X structure does not prevent formation of new TADs but can be further subdivided into new domains by addition of a *rex* site.

Given that each DCC-dependent boundary contains a high-occupancy *rex* site and that a single strong *rex* site is sufficient to create a boundary at a new location on X, we asked whether the high-occupancy *rex* sites that fail to define boundaries can nonetheless reduce DNA interactions between flanking loci. Five *rex* sites that have higher SDC-3 binding than the boundary-forming site *rex-47* failed to form boundaries but did alter chromosome structure. That is, in DCC mutants, interactions between loci flanking these non-boundary *rex* sites increased compared to interactions across neighboring loci (Figures S3B and S3C). DCC binding at these *rex* sites may be insufficient to create strong boundaries due to unknown factors that modulate TAD structure (such as lamin binding at *rex-40*, *rex-45*, and *Prex-30*), or DCC-dependent boundary formation may be overwhelmed by strong DCC-independent boundaries nearby (at *rex-23* and *rex-16*). Regardless of whether a *rex* site defines a boundary, the level of SDC-3 binding at that site correlates strongly with the DCC-dependent change in insulation score (Figure S3B).

We next sequentially inserted three TAD-boundary *rex* sites from the center of X into the center of chromosome I in the *3rexΔ* strain. Inserted *rex* sites recruited the DCC but with only about 20% of the binding of their endogenous X locations (Figure S4C). These inserted *rex* sites had the same spacing as on X but did not create boundaries on chromosome I (Figures

Figure 1. A Single *rex* Site Is Necessary for Formation of Each DCC-Dependent TAD Boundary

(A) Locations on X of the eight *rex* sites (orange) at DCC-dependent TAD boundaries. All eight sites are deleted on *8rexΔ* chromosomes, but only a subset is deleted on *rex-47Δ*, *3rexΔ*(magenta circles) and *6rexΔ* (green asterisks) chromosomes.

(B–D) X chromosome heatmaps binned at 50 kb show wild-type Hi-C Z-scores subtracted from *rex-47Δ* (B), *3rexΔ* (C), or *6rexΔ* (D) Hi-C Z-scores. Red, higher interactions in *rex* mutant. Blue, higher interactions in wild type. Arrows, positions of deleted *rex* sites where TAD boundaries are lost. Plots (below) show insulation scores across X in *rex* deletion mutants (blue) and wild-type embryos (orange) and the insulation score difference between genotypes (red). Blue ticks, positions of deleted *rex* sites. Orange ticks, DCC-dependent boundaries that persist in the mutant.

(E–G) X heatmaps binned at 20 kb show Hi-C interactions in *8rexΔ* (E), DCC mutant [*sdc-2(y93, RNAi)*] (F), and wild-type (G) embryos. Arrows mark positions of DCC-dependent boundaries found in wild-type embryos, which are lost in both mutants. Other DCC-independent boundaries remain.

(H and I) Heatmaps binned at 50 kb compare Hi-C Z-scores in *8rexΔ* (H) or DCC (I) mutants to those in wild-type embryos. Plots (below) show X chromosome insulation profiles. Black arrows (top) and blue ticks (bottom) show locations of DCC-dependent boundaries.

(J) Heatmaps binned at 10 kb show enlargement of the X region surrounding *rex-43* and *rex-48* (arrows) in wild-type and mutant embryos and the interaction between the two *rex* sites in wild-type embryos (circle).

(K) 3D plots show that average Z-scores increase in *8rexΔ* versus wild-type embryos for interactions among the 22 non-boundary *rex* sites with highest SDC-3 binding. Shown are interactions between sites within 4 Mb. DCC-mediated *rex* interactions occur regardless of the orientation of known X-enriched motifs (Jans et al., 2009) that are important in *rex* sites for DCC binding (Figure S3A).

Insulation scores were calculated by summing interactions in a 500 kb sliding window. See also Figures S1–S3 and Tables S1 and S2.

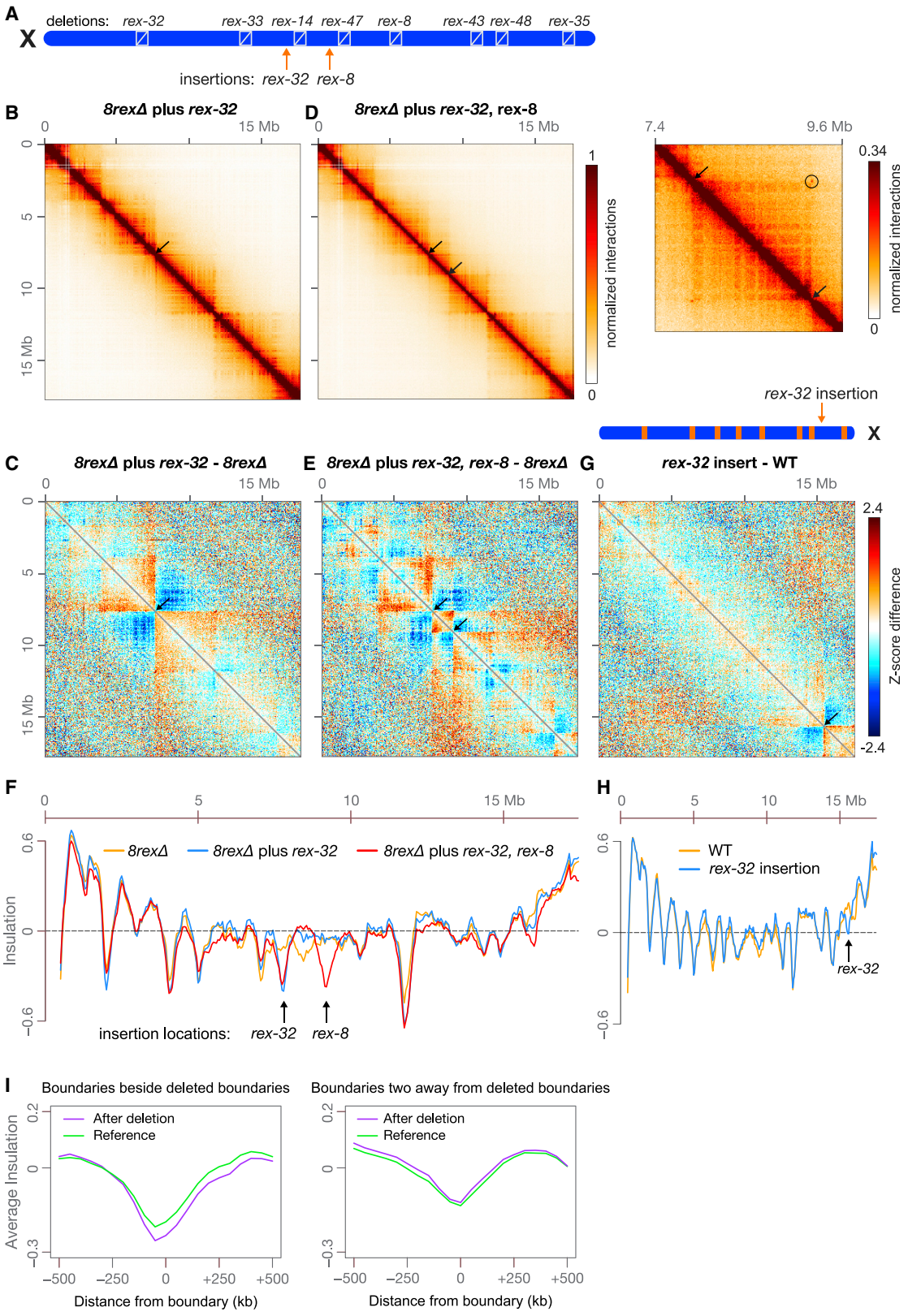

(legend on next page)

S4D–S4F). Lack of new boundaries is consistent with the observation that *rex* sites on X with the same low level of DCC binding as at these ectopic sites do not define TAD boundaries, but we cannot rule out the possibility that some other unique characteristic of X chromosomes, such as widespread DCC binding or H4K20me1 enrichment, is necessary for DCC-dependent boundary formation.

Together, our results establish that the DCC forms boundaries via binding to high-affinity *rex* sites with multiple X-enriched motifs located at boundaries and not through intra-TAD interactions. A single inserted *rex* site is sufficient to define a boundary at a new location on X, and interactions with a second inserted *rex* site do not strengthen the boundary, revealing that interactions between *rex* sites at boundaries are not necessary to form a boundary.

Creating and Destroying Boundaries Affects the Strength of Neighboring and Distant Boundaries

Our deletion series offered a unique setting to investigate how adding and removing boundaries affects the strength of neighboring and distant boundaries. When comparing *8rex⊿* versus *6rex⊿* X chromosomes, we found that the four DCC-independent TAD boundaries flanking the two additional *rex* deletions in *8rex⊿* became stronger (Figure S4G). Overall, composite profiles showed that when a boundary was eliminated, adjacent boundaries were strengthened ($p = 0.02$, paired t test; Figure 2I), while boundaries two away from deleted boundaries showed no consistent pattern of change ($p = 0.60$, Figure 2I).

Conversely, when a new boundary was created, the adjacent boundaries were weakened. For example, when the inserted *rex-32* formed a new TAD boundary in the center of the *8rex⊿* chromosome, the upstream DCC-independent boundary became weaker, and the local minimum in the *8rex⊿* insulation profile downstream of the *rex-32* insertion site disappeared (Figure 2F). Changes in DCC-independent boundary strength caused by altering DCC-dependent boundaries reveal that a boundary can influence the strength of an adjacent boundary even when boundaries are established through different mechanisms.

Boundary deletions can also have long-range effects on the strength of distant boundaries. For example, when *rex* sites were deleted on the right side of X, boundaries were altered over 10 Mb away on the left side of X (Figure S4H). The intricate interplay between distant boundaries highlights the complexity of predicting the long-range effects of altering chromosome structure and suggests the intriguing possibility that perturbation of one site could affect the functions of broad genomic regions.

Most DCC Binding Is Preserved on *8rex⊿* Chromosomes

Assessing the effect of aberrant TAD structure on gene expression in *8rex⊿* embryos required that we understand the degree to which DCC binding along X was affected by *rex* deletions. Thousands of DCC peaks of varying strengths are detectable on X by ChIP-seq analysis (Albritton et al., 2017; Crane et al., 2015). These peaks represent two categories of DCC binding: autonomous, X-motif-dependent binding to *rex* sites and non-autonomous binding to secondary sites that lack X-enriched motifs and exhibit DCC binding only when located on X chromosomes (Albritton et al., 2017; Csankovszki et al., 2004; Ercan et al., 2007; Jans et al., 2009; McDonel et al., 2006; Pferdehirt et al., 2011). *rex* sites confer X chromosome specificity for DCC binding.

To determine whether loss of strong *rex* sites affects DCC binding nearby or broadly, we compared SDC-3 and DPY-27 binding on *8rex⊿* versus wild-type X chromosomes. In *8rex⊿* embryos, DCC binding was preserved at all remaining *rex* sites (Figure S1A). Furthermore, the change in DCC binding across the entire X chromosome was minimal, but the ratio of DCC binding on *8rex⊿* compared to wild-type chromosomes revealed that binding of both DCC components was reduced up to 16-fold immediately adjacent to the *rex* deletions and gradually returned to wild-type levels at approximately 20 kb on either side of each deleted site (Figures S1B and S1C). Similarly, we compared DCC binding around *rex* sites inserted into new locations on *8rex⊿* X chromosomes to binding on *8rex⊿* chromosomes lacking the *rex* insertion. DCC binding was enriched approximately 16-fold around the inserted sites, and binding gradually decreased to wild-type levels approximately 15 kb from the insertions (Figures S1D and S1E). Two explanations could account for the reduction in DCC binding around deleted sites and increase around inserted sites. First, DCC binding at strong *rex* sites might facilitate DCC binding nearby, up to about 20 kb. Alternatively, the sequences within 20 kb of the *rex* site may not be bound directly by the DCC but instead be in close enough proximity to flanking DNA to become crosslinked, thus giving the appearance of increased DCC binding nearby. Because DCC binding was retained on *8rex⊿* X chromosomes beyond 20 kb from each

Figure 2. A High-Occupancy *rex* Site Is Sufficient to Create a TAD Boundary at a New Location on X

(A) Locations on X of eight *rex* deletions and two *rex* insertions at new locations (arrows). *rex-32* was inserted 224 kb from wild-type *rex-14*; *rex-8* was inserted 267 kb from wild-type *rex-47*.

(B and D) Heatmaps binned at 20 kb show Hi-C interactions on X in embryos with either a *rex-32* insertion (B) or *rex-32* and *rex-8* insertions (D). Arrows mark locations of inserted *rex* sites where new TAD boundaries are created. (D, right) Heatmap binned at 10 kb shows enlargement of the X region surrounding the inserted *rex* sites (arrows) and the interaction between the inserted sites (circle).

(C and E) Z-score subtraction heatmaps binned at 50 kb show increased (red) and decreased (blue) interactions on *8rex⊿* chromosomes with *rex* insertions of *rex-32* (C) or *rex-32* and *rex-8* (E) compared to *8rex⊿* chromosomes. Arrows, locations of inserted *rex* sites.

(F) Plot comparing X insulation scores of *8rex⊿* chromosomes (orange) to those of *8rex⊿* chromosomes with one (blue) or two (red) inserted *rex* sites.

(G) Diagram shows the location of *rex-32* inserted 1.05 Mb from *rex-48* on the wild-type X chromosome (arrow). Z-score subtraction heatmap binned at 50 kb shows the difference in Z-scores between *rex-32* insertion and wild-type chromosomes.

(H) Plot comparing X chromosome insulation scores for wild-type (orange) and *rex-32* insertion (blue) embryos.

(I) Boundaries adjacent to deleted boundaries became stronger ($p = 0.02$, paired t test), while boundaries two away were unchanged ($p = 0.60$). Using Hi-C data from *rex-47⊿*, *3rex⊿*, *6rex⊿*, and *8rex⊿* X chromosomes, we calculated the average insulation profile around all boundaries adjacent to a deleted boundary and compared it to the profile at the same boundaries in the strain with the next fewer deletions (see STAR Methods).

See also Figures S3 and S4 and Tables S1 and S2.

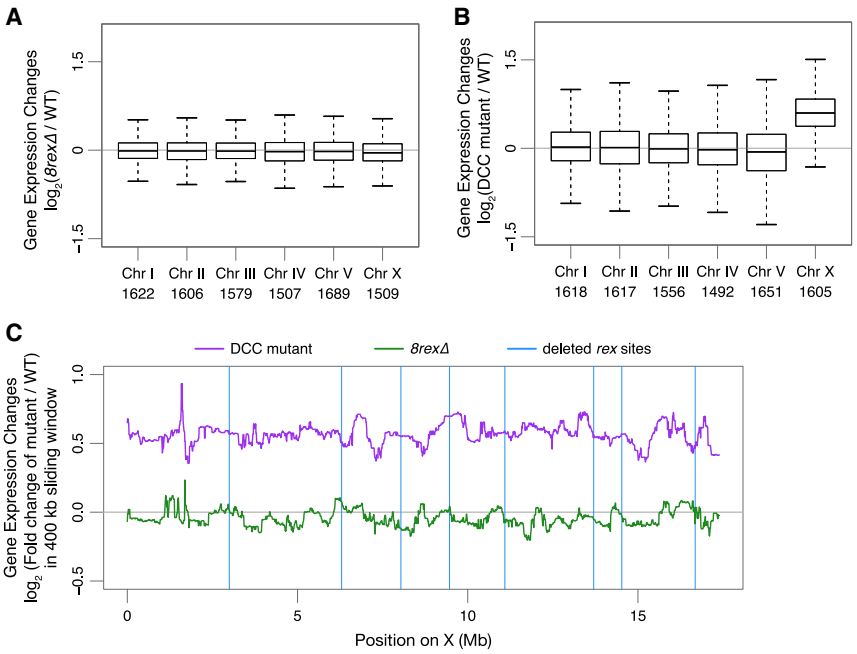

Figure 3. Expression of X-Linked Genes Is Not Significantly Changed by Loss of TAD Boundaries

(A and B) Box plots show gene expression changes for each chromosome in *8rexΔ* (A) or *sdc-2(y93, RNAi)* (B) embryos versus wild-type embryos. Numbers of genes per chromosome are listed.

(C) Median gene expression changes in DCC mutant or *8rexΔ* versus wild-type embryos in a 400 kb sliding window on X. Blue vertical lines, locations of *rex* sites deleted in *8rexΔ*. See also Figure S5 and Table S3.

deleted *rex* site, we could measure the effect of aberrant TAD structure on X gene expression without the complication of a general disruption of DCC binding across X.

TADs Do Not Mediate Transcriptional Repression during Dosage Compensation

To determine whether disruption of TAD structure alters dosage compensation, we first inspected *8rexΔ* worms for evidence of canonical dosage compensation defects. Complete disruption of dosage compensation causes XX-specific embryonic lethality, and weak disruption causes dumpy (Dpy) and egg-laying defective (Egl) phenotypes (Dawes et al., 1999). Dosage compensation defects can also be detected by an even more sensitive genetic assay. Males with *xol-1* mutations are inviable because the DCC binds inappropriately to the single X and represses X expression. They are rescued by mutations that disrupt dosage compensation (Miller et al., 1988; Rhind et al., 1995). *8rexΔ* worms do not display any of these dosage compensation phenotypes. They have a normal brood size, and 100% of animals are viable and not Dpy or Egl (Table S3). Deletions do not rescue *xol-1* mutant males (STAR Methods).

To assay dosage compensation more directly and thoroughly, we measured gene expression genome-wide. We performed RNA sequencing (RNA-seq) on mixed-stage embryos of three genotypes: wild type, a DCC mutant lacking DCC binding on X, and *8rexΔ* in which X topology was altered but the majority of DCC binding persisted.

Assaying embryos allowed us to measure elevation in X expression in the severe DCC mutant before the animals died. However, using embryos required that we carefully match the age distribution of embryos in the populations of different genotypes. X chromosome expression is silenced in the germline (Fong et al., 2002; Kelly et al., 2002; Tzur et al., 2018), and as silencing wanes in early embryos, average expression of genes on X, but not autosomes, increases for approximately the first 5 h of embryogenesis (Figure S5A). Thus, comparing populations of embryos that are not precisely age matched could introduce X-chromosome-wide artifacts in the analysis of transcript levels (Figure S5B). To avoid such confounding factors, we first showed that embryogenesis proceeds at the same rate in *8rexΔ* and wild-type animals (Figure S5C).

For each RNA-seq replicate, we attempted to harvest age-matched embryo populations by growing worms and collecting embryos of all genotypes in parallel. We then computationally compared the age distribution of wild-type and *8rexΔ* embryo populations by assessing expression levels of autosomal genes that change during development (STAR Methods; Figure S5D). We selected the five best-matched wild-type and *8rexΔ* replicates, excluding other replicates in which the wild-type embryos clearly had an older age distribution than the *8rexΔ* population. While median X expression was elevated 1.5-fold in DCC mutant versus wild-type embryos ($p = 2 \times 10^{-16}$, two-sided Wilcoxon rank-sum test comparing changes on X to autosomes), expression of X genes was not elevated in *8rexΔ* embryos (median fold change 0.97 compared to wild type, $p = 0.1$) (Figures 3A and 3B). No individual genes showed significant differential expression between wild-type and *8rexΔ* embryos (false discovery rate [FDR] > 0.06 for all genes).

To determine whether transcription varied with changes in TAD boundaries, we calculated the average change in gene expression in a 400 kb sliding window along X. No correlation was evident between changes in gene expression and distance to a DCC-dependent boundary for either *8rexΔ* or DCC mutant embryos (Figure 3C). The small cohort of genes within 100 kb of an altered boundary did not show dramatic expression differences compared to genes farther from a boundary. These observations reinforce the conclusion that dosage compensation is a chromosome-wide process that represses genes across X regardless of their proximity to TAD boundaries (Crane et al., 2015). In both *8rexΔ* and DCC mutant embryos, X chromosome TAD boundaries were lost, but X-linked expression was elevated only in the DCC mutant and not significantly changed in *8rexΔ*. Therefore, DCC-dependent TADs are neither a cause nor a consequence of transcriptional repression; the changes in chromosome domain architecture and gene expression result from two separate DCC roles.

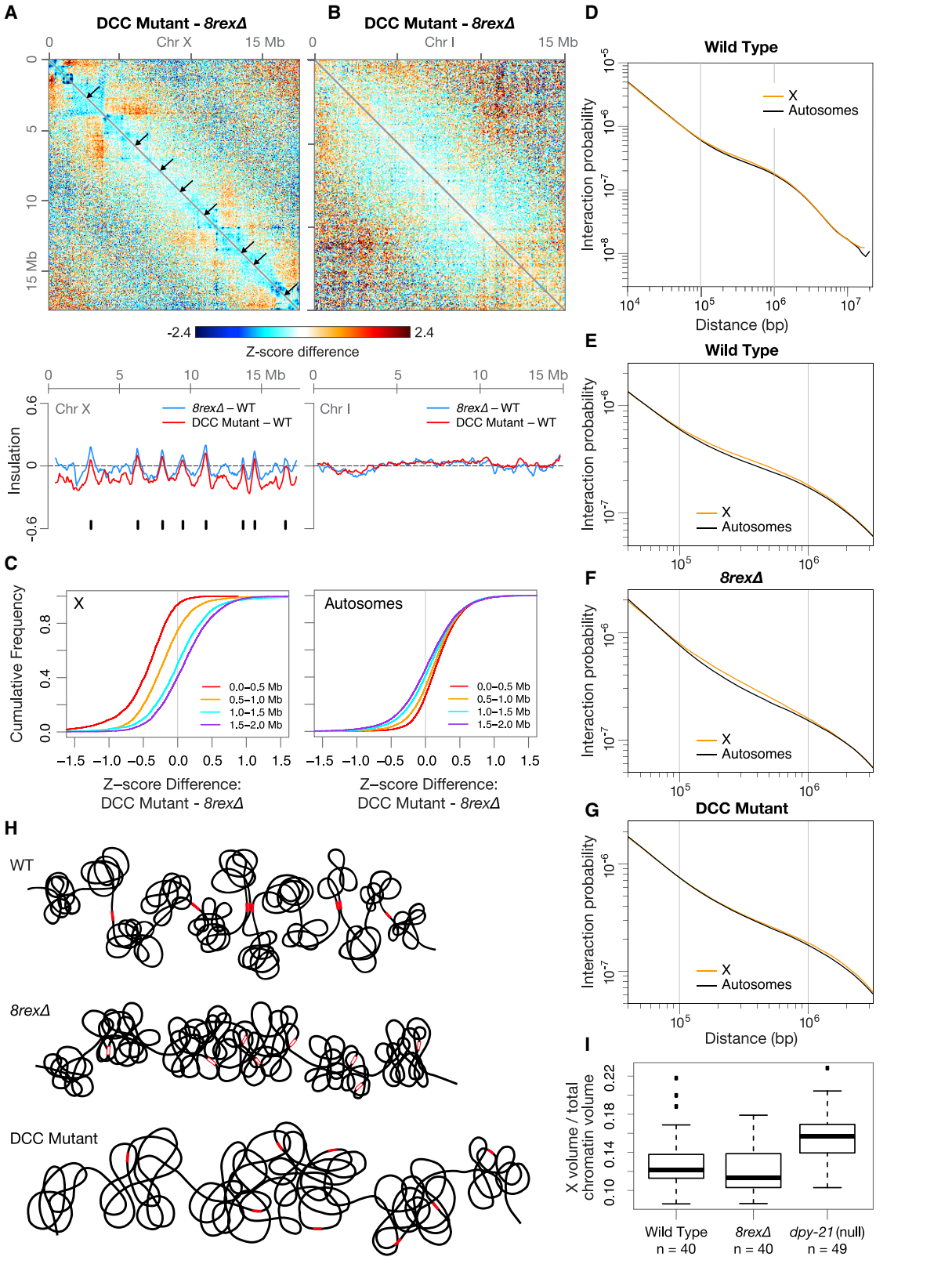

(legend on next page)

The DCC Promotes Interactions at the Scale of 0.1–1 Mb Independently of TAD Boundary Formation

Beyond revealing that dosage compensation occurs without TADs, the complete disruption of DCC-dependent TAD boundaries on *8rex⊿* chromosomes allowed us to discover DCC-dependent structures that persisted in the absence of TADs and could be important for long-range transcriptional repression. By comparing the X topology of *8rex⊿* embryos to DCC mutant embryos, we found that interactions between loci within ~1 Mb were reduced in DCC mutants but persisted across the X chromosome of *8rex⊿* embryos (Figures 4A–4C). The X insulation profile in DCC mutants reflects this chromosome-wide reduction in interactions (Figure 4A). In contrast, the pattern of interactions on autosomes was unchanged between wild-type and either *8rex⊿* or DCC mutant embryos (Figure 4B).

The differences in interactions on X versus autosomes were apparent from plotting the average interaction frequencies between loci at increasing genomic distances. Interaction frequencies scale with genomic distance but have different slopes at different length scales (Figure 4D). This "scaling factor" was shallowest for loci separated by 0.1–1 Mb, and the X chromosome had more interactions than autosomes at these distances, while X and autosomes had matching scaling factors below 0.1 Mb and over 1 Mb (Figure 4E). The 0.1–1 Mb interactions on X were similarly elevated in *8rex⊿* but not DCC mutant embryos, indicating that these interactions occur independent of TADs but are mediated by the DCC (Figures 4F and 4G). Therefore, in addition to creating TAD boundaries, the DCC confers a unique structure on X by promoting interactions at the scale of 0.1–1 Mb (Figure 4H).

Besides creating TADs and increasing interactions between loci in the 0.1–1 Mb range, the DCC compacts the overall volume of X (Brejc et al., 2017; Lau et al., 2014). To determine whether this compaction relies on TAD formation, we measured the volume of X in intestines of wild-type, *8rex⊿*, and *dpy-21*(null) adults using antibodies to the DCC condensin subunit DPY-27 to mark X. *dpy-21*(null) mutations do not block assembly of other DCC subunits onto X but do result in Dpy, viable animals with elevated X chromosome expression (Brejc et al., 2017; Yonker and Meyer, 2003). As shown previously (Brejc et al., 2017; Lau et al., 2014), the volume of X expanded in *dpy-21*(null) versus wild-type animals. In contrast, X volume was unchanged in *8rex⊿* adults (Figure 4I). Therefore, the DCC-mediated compaction of X is unrelated to TAD structure but could reflect the increased chromatin interactions at the 0.1–1 Mb scale and could contribute to dosage compensation. The DCC's dual functions in establishing TAD boundaries and compacting chromatin at the 0.1–1 Mb scale are consistent with a mechanism in which the DCC remodels chromosome topology through loop extrusion (see Discussion).

Loss of DCC-dependent TAD boundaries via *rex* deletions also enabled us to determine whether TADs affect the positioning of X chromosomes within the nucleus. X chromosomes of XX hermaphrodites localize to the nuclear periphery somewhat more frequently than those of either XO males or XX DCC mutants (Snyder et al., 2016), both of which lack DCC binding on X and DCC-dependent TADs. Using DCC immunofluorescence we assessed X positioning in *8rex⊿* and wild-type embryos (Figure S5E). The radial positioning of X within the nucleus was unchanged in *8rex⊿* versus wild-type XX embryos, indicating that DCC-dependent TAD boundaries do not control nuclear positioning of X chromosomes.

Destroying DCC-Dependent TADs Reduces Thermotolerance, Shortens Lifespan, and Accelerates Aging

Although disrupting X structure did not cause statistically significant changes in embryonic gene expression under normal growth conditions, aberrant chromosome architecture did adversely affect the ability of adults to tolerate proteotoxic stress induced by a stressful condition. When worms are exposed to proteotoxic stresses, the presence of unfolded proteins triggers activation of genes needed to refold proteins and restore homeostasis (Higuchi-Sanabria et al., 2018). We assessed the ability of *8rex⊿* adults to tolerate three forms of proteotoxic stress. We heat stressed worms at 37°C during day 1 of adulthood and measured their survival. After 7 h, the survival of *8rex⊿* adults was significantly lower than that of wild-type adults ($p = 0.0014$, paired t test; Figure 5A; Table S4), indicating reduced thermotolerance. We then induced endoplasmic reticulum (ER) unfolded protein stress using tunicamycin, which causes the accumulation of unfolded glycoproteins in the ER, and mitochondrial stress using paraquat, which causes accumulation of reactive oxygen species in mitochondria. *8rex⊿* adults were not more sensitive than wild-type adults to either ER or mitochondrial stress (Figures 5B and 5C; Table S5). Thus, removing DCC-dependent TADs specifically impairs thermotolerance but does not generally compromise responses to all forms of proteotoxic stress. Adults with disrupted X structure may be uniquely sensitive to heat because heat treatment is a systemic stress that affects the whole cell rather than individual organelles.

Figure 4. The DCC Promotes Interactions on X at the Scale of 0.1–1 Mb Independent of TAD Formation

(A and B) Z-score subtraction heatmaps show increased (red) and decreased (blue) interactions for chromosomes X (A) and I (B) in *sdc-2(y93, RNAi)* versus *8rex⊿* embryos. Arrows mark locations of DCC-dependent TAD boundaries, which are present in wild-type embryos, but not in either mutant. Plots (below) show changes in insulation profiles of *8rex⊿* and DCC mutant versus wild-type embryos. Black ticks, DCC-dependent boundaries on X.

(C) Cumulative plots show Z-score differences between DCC mutant and *8rex⊿* chromosomes at different length scales. More interactions within 1 Mb occur on X in *8rex⊿* versus DCC mutant embryos.

(D) Scaling plot shows the average interactions between loci at increasing distances (10 kb–20 Mb) on X and autosomes in wild-type embryos.

(E–G) Scaling plots zoom in on the average interactions between loci within 40 kb–3.2 Mb on X and autosomes in wild-type (E), *8rex⊿* (F), or DCC mutant (G) embryos.

(H) Cartoons of X chromosome structure in three genotypes. Red rectangles, *rex* sites; open rectangles, *rex* deletions. On *8rex⊿* chromosomes, the eight DCC-dependent boundaries found on wild-type chromosomes are lost, while other DCC-mediated interactions and DCC-independent boundaries remain. In DCC mutants, the eight DCC-dependent boundaries are lost, as are the DCC-mediated interactions at the 0.1–1 Mb length scale. X volume expands in DCC mutant, but not in *8rex⊿* embryos.

(I) Boxplots show the fraction of total chromatin (measured by DAPI staining) occupied by X (measured by DPY-27 immunofluorescence) for intestinal nuclei of wild-type, *8rex⊿*, and *dpy-21*(null) adults. X compaction does not require DCC-dependent TAD formation. n, number of nuclei

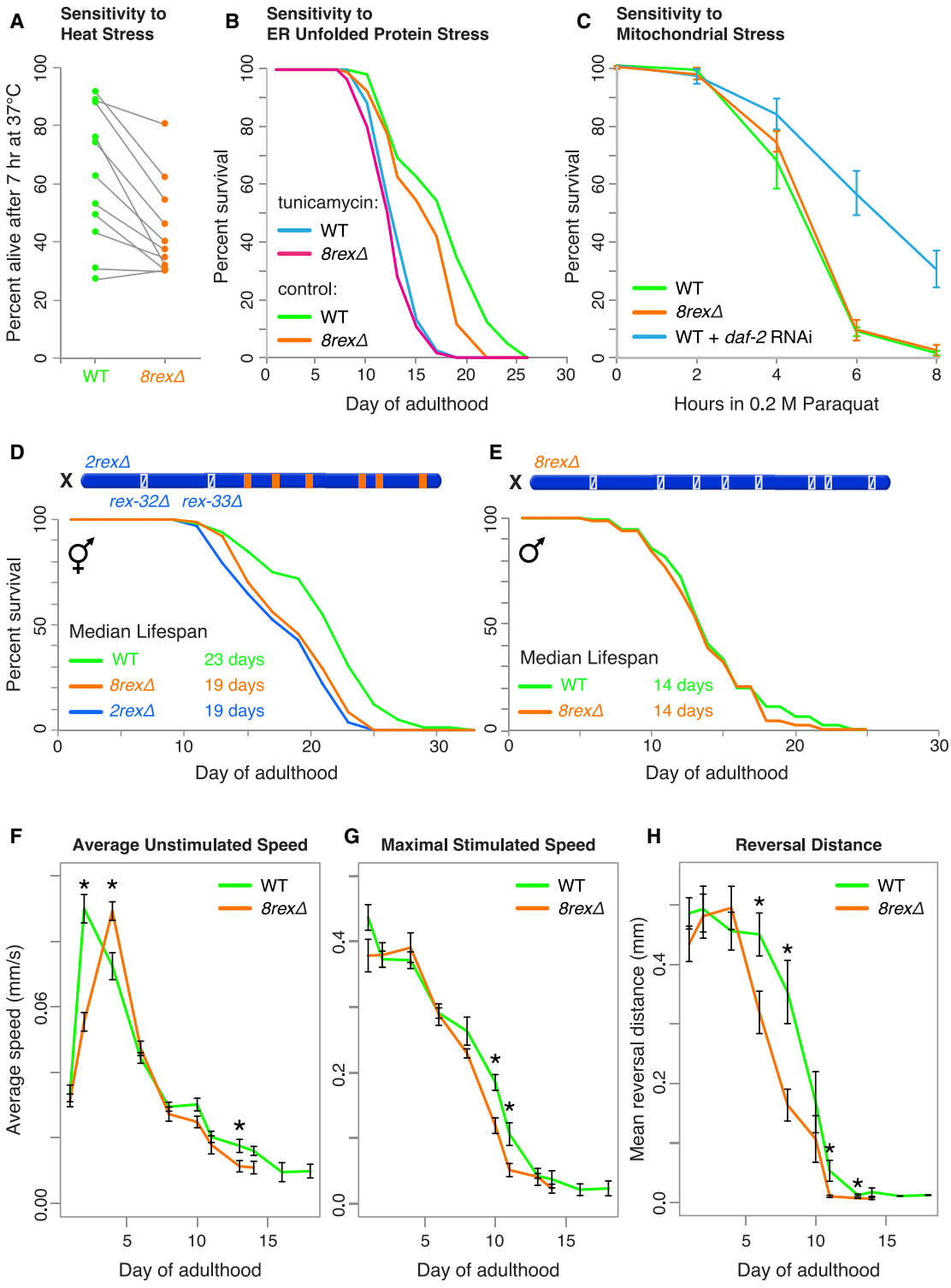

Figure 5. *8rexΔ* Hermaphrodites Exhibit Reduced Thermotolerance, Shortened Lifespan, and Accelerated Aging

(A) Percent survival of 50 wild-type or *8rexΔ* day 1 adult worms after 7 h at 37°C in each of nine trials shows reduced thermotolerance in *8rexΔ* adults. A gray line links the measurements of the two genotypes in the same trial.

(B) Lifespans were scored for wild-type and *8rexΔ* hermaphrodites transferred on day 1 of adulthood to plates with either 1% DMSO (control) or 20 ng/μL tunicamycin to induce ER unfolded protein stress. Replicate experiments and statistics are in Table S5.

(legend continued on next page)

To assess whether *rex* deletions affect other aspects of adult worm performance, we measured the lifespan of *8rexΔ* animals. Median lifespan of *8rexΔ* hermaphrodites was 19 days, compared to 23 days for wild-type hermaphrodites (Figure 5D; Table S6; see also Figure 5B). This significant lifespan decrease ($p < 0.0001$, log rank test) is comparable to that caused by disrupting known regulators (*xbp-1*, *ire-1*, and *daf-16*) of stress responses and lifespan (Calo et al., 2018; Henis-Korenblit et al., 2010; Lin et al., 2001; Taylor and Dillin, 2013).

Because the DCC and *rex* sites function specifically in hermaphrodites, not males, to control X chromosome architecture and gene expression, males are not affected by mutations that disrupt these dosage compensation components. Therefore, if the decrease in hermaphrodite lifespan is a *bona fide* consequence of disrupting sex-specific, DCC-dependent functions of *rex* sites, the lifespan of males should not be affected by *rex* deletions. Indeed, lifespans of *8rexΔ* and wild-type males were not significantly different (median 14 days, $p = 0.25$), indicating that the lifespan defect of *8rexΔ* hermaphrodites is sex dependent and DCC dependent (Figure 5E). The reduction in lifespan is not explained by defects in DCC-independent processes caused by either *rex* deletions or off-target mutations introduced during deletion of *rex* sites.

To determine whether *8rexΔ* worms die prematurely from accelerated aging rather than general "sickness" throughout development, we measured locomotory behaviors in adult animals using a Multi-Worm Tracker (Swierczek et al., 2011). We first asked whether locomotion declines at the same rate in *8rexΔ* mutants and in wild-type animals as a function of age. Hermaphrodite *8rexΔ* worms moved normally at day 1 of adulthood, but after a peak in speed comparable to that in wild-type animals, their movement subsequently declined more rapidly than did that of wild-type worms. The decline was evident in both the speed of normal explorative movement in the absence of a stimulus and the speed of movement in response to a controlled mechanical tap stimulus (Figures 5F, 5G, S6A, and S6B). A tap elicits a multifaceted escape response: worms increase their speed, reverse the direction of motion, and then turn. By two metrics, speed and distance traveled backward, the escape response declined more rapidly during adulthood in *8rexΔ* mutants than in wild-type animals (Figures 5G and 5H).

We also monitored animal size during adulthood. Wild-type animals increase in size for the first 6 days of adulthood and then shrink. Shorter-lived wild-type individuals are smaller and stop growing sooner (Hulme et al., 2010; Pincus et al., 2011). Although the *8rexΔ* mutants were the same size as wild-type animals at adult day 1 and increased in size somewhat until day 6, they never reached the same size as wild-type animals, and they shrank in size faster (Figure S6C).

The more rapid decline in explorative locomotive speed, maximal escape speed, magnitude of escape response, and body size despite all of these metrics being similar between young adult *8rexΔ* and wild-type worms, indicates that *8rexΔ* worms are healthy at the onset of adulthood but have a rapid-aging phenotype. These results suggest that although aberrant chromosome structure does not affect DCC-dependent gene expression early in development, it does cause misregulation of the aging program later in life.

The reduced thermotolerance and accelerated aging could be due to changes in expression of a few genes on X with roles in these processes. Alternatively, the phenotypes could result from the cumulative effect of misregulating many genes across X, as in aneuploid cells in which overexpression of genes from an entire chromosome causes proteotoxic stress regardless of the specific aneuploid chromosome (Oromendia and Amon, 2014). To distinguish between these possibilities, we measured lifespans and stress responses of adults with subsets of the eight *rex* deletions.

The full reduction in lifespan observed in *8rexΔ* was seen when only *rex-32* and *rex-33* were deleted at the leftmost two boundaries (*2rexΔ*) (Figure 5D; Table S6). Deleting the six other *rex* sites had no effect on lifespan (Figure S6D; Table S6). Furthermore, the reduction in lifespan was not suppressed by establishing new DCC-dependent boundaries in the center of X by inserting *rex* sites (Figure S6E; Table S6). Therefore, the aging defect is likely caused by misregulation of specific genes required for normal lifespan rather than the cumulative consequence of many changes in gene expression across the entire chromosome. Deleting *rex-32* or *rex-33* individually did not recapitulate the lifespan reduction caused by deleting two sites together (Figure S6F), suggesting that misregulation of multiple genes is responsible for lifespan reduction of *8rexΔ* animals. The misregulated genes are likely to be in proximity to *rex-32* and *rex-33*, although other genes on X could also be responsible, given that *rex* deletions can modulate the strength of distant boundaries.

In contrast to the lifespan results, both *2rexΔ* and *6rexΔ* adults behaved like *8rexΔ* adults in having reduced thermotolerance compared to wild-type adults ($p = 0.004$ and $p = 0.002$, respectively, paired t test) (Figure S6G and S6H; Table S4). The thermosensitivity of *2rexΔ*, *6rexΔ*, and *8rexΔ* adults was not increasingly more severe with removal of additional *rex* sites. Rather, the thermosensitivity was not different among the three genotypes ($p > 0.6$ for each pairwise comparison, Table S4).

(C) Percent survival of day 1 adult wild-type and *8rexΔ* hermaphrodites in 0.2 M paraquat to induce reactive oxygen species in mitochondria. Wild-type worms subjected to *daf-2* RNAi were used as a control for increased oxidative stress tolerance. For each genotype, the average of at least three replicates is plotted. Error bars, standard error of the mean (SEM).

(D) Comparison of lifespans for wild-type versus *8rexΔ* ($p < 0.0001$, logrank test) and *2rexΔ* ($p < 0.0001$) hermaphrodites shows lifespan shortening in mutants. See replicate experiments and statistics in Table S6.

(E) Comparison of lifespans for wild-type versus *8rexΔ* males ($p = 0.2485$, log rank test).

(F) Average unstimulated speed of wild-type and *8rexΔ* hermaphrodites during aging. For each genotype, the speed of 50 worms on each of eight replicate plates was measured throughout adulthood. Measurements included only moving worms. We calculated the mean speed of worms on each plate and plotted the mean ± SEM of all eight plates. Asterisks, significant differences ($p < 0.05$, t test). mm/s, millimeters per second.

(G and H) Maximal speed (G) and reversal distance (H) during aging of wild-type and *8rexΔ* hermaphrodites in response to a mechanical stimulus (plate tap). Mean ± SEM are plotted as in (F).

See also Figure S6 and Tables S4–S6.

Thus, thermosensitivity appears to be similarly influenced by misregulation of genes in different regions of X rather than the cumulative misregulation of many genes all across X. Neither *6rexΔ* nor *2rexΔ* adults were more sensitive to ER or mitochondrial stress compared to *8rexΔ* or wild-type adults (Table S5; Figures S6I and S6J).

Candidates for the misregulated genes that cause reduced heat tolerance and accelerated aging include genes that are induced in response to heat shock and genes that regulate aging. In a recent genome-wide study, of 815 genes upregulated in wild-type worms after heat shock (Brunquell et al., 2016), 149 genes were on X. In addition, genetic screens identified 22 genes on X that either extend worm lifespan or cause accelerated aging when knocked down, including six genes in the TADs flanking *rex-32* and *rex-33* (Hamilton et al., 2005; Hansen et al., 2005; Samuelson et al., 2007). Although none of these candidate genes on X exhibited significant differential expression in *8rexΔ* embryos, their misregulation in *8rexΔ* adults upon heat shock or during aging might contribute to the defective heat shock response and accelerated aging. Reduced thermotolerance, shortened lifespan, and accelerated aging resulting from disrupted chromosome architecture are likely caused by the combined effect of misregulating multiple candidate genes.

DISCUSSION

Metazoan chromosomes are organized into megabase-scale TADs, but the mechanisms that establish these domains and their link to gene expression remain unclear. We discovered the requirements for establishing hermaphrodite-specific TAD boundaries during *C. elegans* dosage compensation. Unlike other studies that abolished TAD structure genome-wide by depleting a protein that is essential for boundary formation and also plays other roles in gene expression and development, our study eliminated DCC-dependent TAD boundaries across X by deleting a series of DCC binding sites. We discovered that removing the single *rex* site at each of eight DCC-dependent boundaries eliminated the boundary. Moreover, inserting a single *rex* site into a new location on X created a TAD boundary. Thus, DCC binding at high-occupancy *rex* sites defines locations of TAD boundaries. By disrupting TAD structure on X while leaving most DCC binding intact, we found that TAD boundaries are neither the cause nor consequence of transcriptional repression during dosage compensation. We also discovered a feature of DCC-mediated chromosome structure that is not reliant on DCC-dependent TAD boundaries and potentially enables long-range gene repression: the DCC promotes DNA interactions at the scale of 0.1–1 Mb. Although *rex* deletions that abrogate TAD structure in hermaphrodites do not affect dosage compensation, they increase thermosensitivity, accelerate aging, and shorten lifespan, implying a role for chromosome architecture in the regulation of stress responses and aging.

Mechanism of TAD Boundary Formation

Our discovery that a single high-occupancy *rex* site is necessary and sufficient to define the location of a DCC-dependent TAD boundary distinguishes between models for establishing TAD boundaries. Boundary locations are not defined passively by intra-TAD interactions. Furthermore, although strong interactions are often observed between DCC-dependent boundaries in *C. elegans* and between adjacent boundaries in mammalian cells, we show that boundary formation does not require boundary-to-boundary interactions.

Instead of favoring a model in which specific DCC-mediated interactions promote TAD boundary formation, our results support the loop extrusion model for boundary formation and chromosome compaction. In this model, a complex extrudes a chromatin loop of increasing size until it reaches a barrier element, which blocks the progression of extrusion (Fudenberg et al., 2016). The loops created by extruders loading across an entire chromosome manifest in Hi-C measurements as increased DNA interactions. Because loops do not cross extrusion barriers, the barriers delineate boundaries between TADs. In mammalian cells, evidence points to the SMC complex cohesin acting as a loop extruder and the DNA-bound protein CTCF acting as a barrier to extrusion (Fudenberg et al., 2018; Sanborn et al., 2015). The related SMC complex condensin can extrude DNA loops *in vitro*, suggesting its role as a loop extruder *in vivo* (Ganji et al., 2018).

Our results fulfill all predictions for the DCC, a condensin complex, acting as a loop extruder *in vivo* and the eight high-occupancy *rex* sites with multiple binding motifs acting as extrusion barriers. First, eliminating the loop extruder should cause TAD boundary loss and an overall reduction in DNA interactions (Fudenberg et al., 2018). Strong interactions between TAD boundaries that can result from loop extrusion should also be lost in the absence of the loop extruder. Indeed, mutations preventing the DCC from binding to X had all these consequences. Second, eliminating a single extrusion barrier should eliminate the boundary. Each *rex* deletion did abolish the associated boundary. Third, removing all extrusion barriers should eliminate TADs but leave other DCC-mediated interactions intact. Indeed, TAD boundaries were lost in *8rexΔ* embryos, but DCC-dependent 0.1–1 Mb interactions on X were retained. Finally, inserting an extrusion barrier at a new location should delineate a new boundary. Insertion of a *rex* site at three new locations on X did define a new boundary at each site.

Under the loop extrusion model, different DCC components would function to extrude loops and block extrusion, analogous to the roles played by cohesin and CTCF during boundary formation in mammalian cells. DCC condensin subunits would extrude chromatin loops, and non-condensin DCC subunits such as SDC-2 would bind *rex* sites and halt extrusion (Figures 6A and 6B). SDC-2, the only DCC subunit with hermaphrodite-specific expression, is essential for robust binding of all DCC components to X and can bind *rex* sites in the absence of other DCC subunits (Albritton et al., 2017; Dawes et al., 1999; Pferdehirt et al., 2011). Thus, SDC-2 could be responsible both for loading the DCC onto X at all *rex* sites and *rex*-dependent secondary sites (as NIPBL loads cohesin) and for binding the highest-affinity *rex* sites in a manner that blocks loop extrusion (as CTCF apparently blocks cohesin extrusion). In principle, SDC-2 could travel with DCC condensin from loading sites on X to the highest-affinity *rex* sites where SDC-2 binds most stably and blocks extrusion. Alternatively, because SDC-2 can bind *rex* sites independently of condensin, and condensin can bind secondary sites on X at a low level in the absence of SDC-2 (Albritton et al., 2017; Pferdehirt et al., 2011), condensin alone could

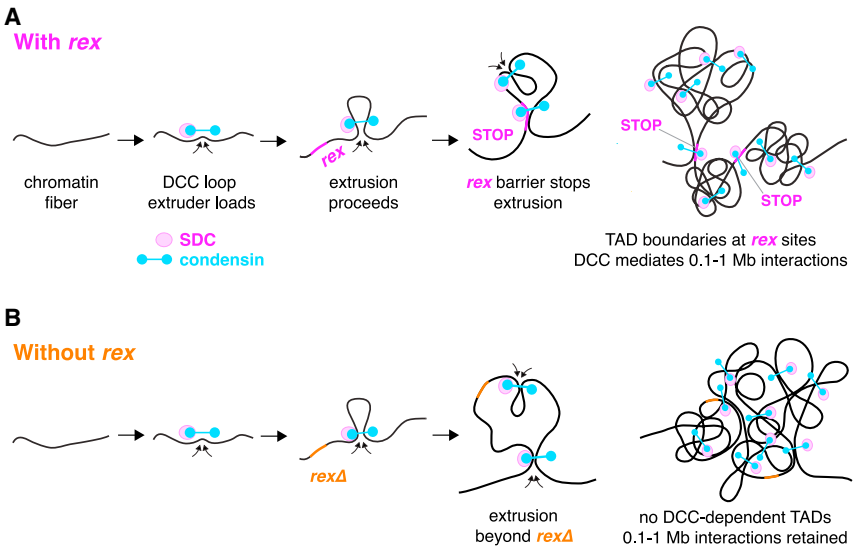

Figure 6. Model for TAD Formation by the DCC

(A) DCC condensin (blue) loads onto chromatin with SDC proteins (magenta) and extrudes loops of increasing size until the extrusion is halted by binding to a high-occupancy *rex* site with multiple X-enriched motifs (pink). Because DCC-mediated loops do not cross high-occupancy *rex* sites, the *rex* sites define the locations of TAD boundaries. The SDC loading factors could travel with condensin subunits from loading sites on X to the highest-affinity *rex* sites where they bind stably and block extrusion. Alternatively, condensin alone could bind at low levels to X and extrude loops until encountering SDC proteins bound independently at a *rex* site. Both possibilities could occur. Only the boundary *rex* sites are shown, even though *rex* sites with a range of DCC binding affinities act as loading sites and confer X specificity.

(B) When high-occupancy *rex* sites are deleted (orange), TAD boundaries are lost, but other DCC-mediated interactions remain, most notably those at the 0.1–1 Mb length scale. The *8rexΔ* X maintains the same level of compaction as the wild-type X.

extrude a loop until encountering SDC-2 bound at a *rex* site. A combination of both options might occur.

A loop extrusion model for DCC progression along X chromosomes also provides an explanation for how the DCC subunit DPY-21, a histone H4K20me2 demethylase, enriches H4K20me1 across X. DPY-21 could associate with the condensin complex, as it extrudes DNA loops, providing access for DPY-21 to demethylate H4K20me2 at all loci across X regardless of proximity to high-occupancy DCC binding sites.

In mammalian cells, pairs of CTCF binding sites that interact strongly tend to contain CTCF binding motifs oriented in a convergent direction (de Wit et al., 2015; Rao et al., 2014; Sanborn et al., 2015). In contrast, high-occupancy *C. elegans rex* sites within 2 Mb interact strongly, regardless of the orientations of their binding motifs (Figure S3A).

TADs and Transcription

Because the DCC can act over a long range to repress transcription on X, DCC-dependent TAD organization was an attractive model for mediating the long-range, chromosome-wide dosage compensation process. However, we found that TAD structure itself does not repress or activate transcription in the context of dosage compensation.

In mammalian cells, loss of a TAD boundary can change transcription by allowing enhancers to ectopically activate genes that were previously in separate TADs (Lupiáñez et al., 2015; Valton and Dekker, 2016), but this mode of regulation by TAD boundaries is likely limited to a few specific genes. Studies that eliminated TADs genome-wide by depleting cohesin, the cohesin loader NIPBL, or CTCF revealed that hundreds of genes had modest increases or decreases in expression but found no widespread ectopic activation (Nora et al., 2017; Rao et al., 2017; Schwarzer et al., 2017). Similarly, we found no broad activation of genes on the *C. elegans* X chromosome when TADs were eliminated. Mechanisms involving ectopic activation of a gene by an enhancer in an adjacent TAD after boundary disruption may not be relevant in *C. elegans*. Although putative enhancers have been identified (Chen et al., 2013; Daugherty et al., 2017; Jänes et al., 2018), no regulatory elements are known to activate gene expression at distances greater than 5 kb.

Our study separates the consequences of eliminating TAD boundaries from other defects caused by removing multifunctional architectural proteins. Interpreting the effects of depleting proteins essential for TAD boundary formation is difficult because the proteins also bind sites outside of TAD boundaries and likely alter gene expression through multiple mechanisms. For example, the majority of genes whose expression in mouse embryonic stem cells was reduced by CTCF depletion had CTCF binding near their transcription start sites, suggesting that CTCF may activate gene expression by binding promoters rather than by establishing TADs (Nora et al., 2017). We found that binding of an architectural protein indeed has distinct functions at different genomic locations. DCC binding to *rex* sites at TAD boundaries is necessary for the creation of boundaries, but DCC binding at other locations is sufficient for transcriptional repression.

TAD-Independent DCC-Mediated Architecture

By comparing X chromosome structure in *8rexΔ* versus DCC mutant embryos, we found that the DCC also promotes chromatin interactions at the 0.1–1 Mb length scale (as expected from a loop extrusion model for condensin action). Loss of these interactions in the DCC mutant is consistent with the effect of removing SMC complexes in other contexts. Loss of cohesin loading in mouse cells and loss of condensin in yeast both result in reduced interactions at distances below 200 kb (Paul et al., 2018; Schwarzer et al., 2017).

The DCC-mediated interactions at the hundred-kb scale are a plausible driver of transcriptional repression because they occur chromosome-wide, consistent with the degree of repression not being correlated with a gene's distance from a *rex* site or TAD boundary (Crane et al., 2015; Jans et al., 2009; Wheeler et al., 2016) (Figure 3). Perhaps the increased interactions are

indicative of the DCC creating an X chromosome compartment with an environment unfavorable for polymerase recruitment. If the DCC-mediated interactions at the 100 kb scale drive dosage compensation, then repression is achieved not by loops between specific loci but through a dynamic ensemble of loops that varies between individual cells and requires DCC binding across the chromosome, not only at *rex* sites.

Chromosome Structure, Lifespan, and Stress Responses

Although aberrant TAD structure does not compromise dosage compensation in embryos, it does reduce lifespan and thermotolerance, suggesting that chromosome structure influences gene regulation in adults. The *8rex⊿* phenotypes could be a cumulative effect of subtle changes in many genes across X that collectively disrupt proteostasis, making worms less able to tolerate heat stress and aging. However, our finding that the reduced lifespan is due to deletion of the two left-most boundary *rex* sites, but not the other six boundary *rex* sites, favors the idea that a few specific genes in proximity to *rex-32* and *rex-33* are responsible for accelerated aging. Moreover, the observation that adults with only two or six *rex* deletions are as thermosensitive as *8rex⊿* adults suggests that thermosensitivity likewise results from misregulation of specific genes in discrete regions of X. In addition, *8rex⊿* worms were not sensitive to other proteotoxic stresses, including mitochondrial stress and ER unfolded protein stress, further suggesting that *rex* deletions do not generally misregulate gene expression chromosome wide and thereby disrupt proteostasis. Our discoveries demonstrate the importance of using whole organisms to dissect the function of chromosome structure during different stages of development and offer new directions for understanding the regulation of lifespan and the connection between chromosome organization and gene regulation.

STAR★METHODS

Detailed methods are provided in the online version of this paper and include the following:

- KEY RESOURCES TABLE
- LEAD CONTACT AND MATERIALS AVAILABILITY
- EXPERIMENTAL MODEL AND SUBJECT DETAILS
  - *C. elegans* Strains
- METHOD DETAILS
  - *rex* Deletions and Insertions
  - Hi-C and Analysis
  - ChIP-seq
  - ChIP-seq Analysis
  - ChIP-qPCR
  - Measuring X Chromosome Volume
  - Measurements of X Chromosome Nuclear Position
  - RNA-seq Library Preparation and Analysis
  - *xol-1* Rescue
  - Imaging the Timing of Embryogenesis
  - Thermotolerance
  - Sensitivity to Mitochondrial Stress
  - Lifespan Analysis
  - Worm Tracking
- QUANTIFICATION AND STATISTICAL ANALYSIS
- DATA AND CODE AVAILABILITY

SUPPLEMENTAL INFORMATION

Supplemental Information can be found online at https://doi.org/10.1016/j.devcel.2019.08.004.

ACKNOWLEDGMENTS

We thank D. Stalford for assistance with figures; S. Uzawa for measurements of X chromosome position; A. Uebersohn for viability measurements; A. Goloborodko for advice on Hi-C analysis; and T. Cline, J. Dekker, G. Fudenberg, G. Karpen, E. Nora, J. Rine, and the Meyer lab for discussions. This work used the Vincent J. Coates Genomics Sequencing Laboratory at U.C. Berkeley, supported by NIH S10 OD018174 Instrumentation Grant. R.H.S was supported by NIH, United States, grant 5F32AG053023 and a Glenn Foundation, United States, for Aging Postdoctoral Fellowship. K.P. and C.K. were supported by Calico Life Sciences. B.J.M. was supported in part by NIH grants R01 GM030702 and R35 GM131845. B.J.M. and A.D. are investigators of the Howard Hughes Medical Institute.

AUTHOR CONTRIBUTIONS

E.C.A., P.A.F., R.H.-S., Q.Y., Q.B., K.P., and A.S. performed experiments and analyzed data. E.C.A. and B.J.M. wrote the paper. All authors designed experiments and edited the paper. B.J.M. guided the study.

DECLARATION OF INTERESTS

The authors declare no competing interests.

Received: March 26, 2019
Revised: June 26, 2019
Accepted: August 6, 2019
Published: September 5, 2019

REFERENCES

Albritton, S.E., Kranz, A.L., Winterkorn, L.H., Street, L.A., and Ercan, S. (2017). Cooperation between a hierarchical set of recruitment sites targets the X chromosome for dosage compensation. eLife *6*, e23645.

Bian, Q., Anderson, E.C., Brejc, K., and Meyer, B.J. (2018). Dynamic control of chromosome topology and gene expression by a chromatin modification. Cold Spring Harb. Symp. Quant. Biol. *82*, 034439.

Brejc, K., Bian, Q., Uzawa, S., Wheeler, B.S., Anderson, E.C., King, D.S., Kranzusch, P.J., Preston, C.G., and Meyer, B.J. (2017). Dynamic control of X chromosome conformation and repression by a histone H4K20 demethylase. Cell *171*, 85–102.e23.

Brunquell, J., Morris, S., Lu, Y., Cheng, F., and Westerheide, S.D. (2016). The genome-wide role of HSF-1 in the regulation of gene expression in *Caenorhabditis elegans*. BMC Genomics *17*, 559.

Calo, E., Gu, B., Bowen, M.E., Aryan, F., Zalc, A., Liang, J., Flynn, R.A., Swigut, T., Chang, H.Y., Attardi, L.D., et al. (2018). Tissue-selective effects of nucleolar stress and rDNA damage in developmental disorders. Nature *554*, 112–117.

Chen, R.A.-J., Down, T.A., Stempor, P., Chen, Q.B., Egelhofer, T.A., Hillier, L.W., Jeffers, T.E., and Ahringer, J. (2013). The landscape of RNA polymerase II transcription initiation in *C. elegans* reveals promoter and enhancer architectures. Genome Res. *23*, 1339–1347.

Chuang, P.T., Albertson, D.G., and Meyer, B.J. (1994). DPY-27: A chromosome condensation protein homolog that regulates *C. elegans* dosage compensation through association with the X chromosome. Cell *79*, 459–474.

Crane, E., Bian, Q., McCord, R.P., Lajoie, B.R., Wheeler, B.S., Ralston, E.J., Uzawa, S., Dekker, J., and Meyer, B.J. (2015). Condensin-driven remodelling of X chromosome topology during dosage compensation. Nature *523*, 240–244.

Csankovszki, G., McDonel, P., and Meyer, B.J. (2004). Recruitment and spreading of the *C. elegans* dosage compensation complex Along X chromosomes. Science *303*, 1182–1185.

Daugherty, A.C., Yeo, R.W., Buenrostro, J.D., Greenleaf, W.J., Kundaje, A., and Brunet, A. (2017). Chromatin accessibility dynamics reveal novel functional enhancers in *C. elegans*. Genome Res. *27*, 2096–2107.

Dawes, H.E., Berlin, D.S., Lapidus, D.M., Nusbaum, C., Davis, T.L., and Meyer, B.J. (1999). Dosage compensation proteins targeted to X chromosomes by a determinant of hermaphrodite fate. Science *284*, 1800–1804.

de Wit, E., Vos, E.S.M., Holwerda, S.J.B., Valdes-Quezada, C., Verstegen, M.J.A.M., Teunissen, H., Splinter, E., Wijchers, P.J., Krijger, P.H.L., and de Laat, W. (2015). CTCF binding polarity determines chromatin looping. Mol. Cell *60*, 676–684.

Dixon, J.R., Selvaraj, S., Yue, F., Kim, A., Li, Y., Shen, Y., Hu, M., Liu, J.S., and Ren, B. (2012). Topological domains in mammalian genomes identified by analysis of chromatin interactions. Nature *485*, 376–380.

Ercan, S., Giresi, P.G., Whittle, C.M., Zhang, X., Green, R.D., and Lieb, J.D. (2007). X chromosome repression by localization of the *C. elegans* dosage compensation machinery to sites of transcription initiation. Nat. Genet. *39*, 403–408.

Farboud, B., and Meyer, B.J. (2015). Dramatic enhancement of genome editing by CRISPR/Cas9 Through improved guide RNA design. Genetics *199*, 959–971.

Farboud, B., Severson, A.F., and Meyer, B.J. (2019). Strategies for efficient genome editing using CRISPR-Cas9. Genetics *211*, 431–457.

Fong, Y., Bender, L., Wang, W., and Strome, S. (2002). Regulation of the different chromatin states of autosomes and X chromosomes in the germ line of *C. elegans*. Science *296*, 2235–2238.

Franke, M., Ibrahim, D.M., Andrey, G., Schwarzer, W., Heinrich, V., Schöpflin, R., Kraft, K., Kempfer, R., Jerković, I., Chan, W.L., et al. (2016). Formation of new chromatin domains determines pathogenicity of genomic duplications. Nature *538*, 265–269.

Fudenberg, G., Abdennur, N., Imakaev, M., Goloborodko, A., and Mirny, L.A. (2018). Emerging evidence of chromosome folding by loop extrusion. Cold Spring Harb. Symp. Quant. Biol. *82*, 034710.

Fudenberg, G., Imakaev, M., Lu, C., Goloborodko, A., Abdennur, N., and Mirny, L.A. (2016). Formation of chromosomal domains by loop extrusion. Cell Rep. *15*, 2038–2049.

Ganji, M., Shaltiel, I.A., Bisht, S., Kim, E., Kalichava, A., Haering, C.H., and Dekker, C. (2018). Real-time imaging of DNA loop extrusion by condensin. Science *360*, 102–105.

Gibcus, J.H., and Dekker, J. (2013). The hierarchy of the 3D genome. Mol. Cell *49*, 773–782.

Gibcus, J.H., Samejima, K., Goloborodko, A., Samejima, I., Naumova, N., Nuebler, J., Kanemaki, M.T., Xie, L., Paulson, J.R., Earnshaw, W.C., et al. (2018). A pathway for mitotic chromosome formation. Science *359*, eaao6135.

Hamilton, B., Dong, Y., Shindo, M., Liu, W., Odell, I., Ruvkun, G., and Lee, S.S. (2005). A systematic RNAi screen for longevity genes in *C. elegans*. Genes Dev. *19*, 1544–1555.

Hansen, M., Hsu, A.L., Dillin, A., and Kenyon, C. (2005). New genes tied to endocrine, metabolic, and dietary regulation of lifespan from a *Caenorhabditis elegans* genomic RNAi screen. PLoS Genet. *1*, 119–128.

Hashimshony, T., Feder, M., Levin, M., Hall, B.K., and Yanai, I. (2015). Spatiotemporal transcriptomics reveals the evolutionary history of the endoderm germ layer. Nature *519*, 219–222.

Henis-Korenblit, S., Zhang, P., Hansen, M., McCormick, M., Lee, S.J., Cary, M., and Kenyon, C. (2010). Insulin/IGF-1 signaling mutants reprogram ER stress response regulators to promote longevity. Proc. Natl. Acad. Sci. USA *107*, 9730–9735.

Higuchi-Sanabria, R., Frankino, P.A., Paul, J.W., Tronnes, S.U., and Dillin, A. (2018). A futile battle? Protein quality control and the stress of aging. Dev. Cell *44*, 139–163.

Hirano, T. (2016). Condensin-based chromosome Organization from Bacteria to Vertebrates. Cell *164*, 847–857.

Hocquet, C., Robellet, X., Modolo, L., Sun, X.M., Burny, C., Cuylen-Haering, S., Toselli, E., Clauder-Münster, S., Steinmetz, L., Haering, C.H., et al. (2018). Condensin controls cellular RNA levels through the accurate segregation of chromosomes instead of directly regulating transcription. eLife *7*, e38517.

Hulme, S.E., Shevkoplyas, S.S., McGuigan, A.P., Apfeld, J., Fontana, W., and Whitesides, G.M. (2010). Lifespan-on-a-chip: microfluidic chambers for performing lifelong observation of *C. elegans*. Lab Chip *10*, 589–597.

Imakaev, M., Fudenberg, G., McCord, R.P., Naumova, N., Goloborodko, A., Lajoie, B.R., Dekker, J., and Mirny, L.A. (2012). Iterative correction of Hi-C data reveals hallmarks of chromosome organization. Nat. Methods *9*, 999–1003.

Jänes, J., Dong, Y., Schoof, M., Serizay, J., Appert, A., Cerrato, C., Woodbury, C., Chen, R., Gemma, C., Huang, N., et al. (2018). Chromatin accessibility dynamics across *C. elegans* development and ageing. eLife *7*, e37344.

Jans, J., Gladden, J.M., Ralston, E.J., Pickle, C.S., Michel, A.H., Pferdehirt, R.R., Eisen, M.B., and Meyer, B.J. (2009). A condensin-like dosage compensation complex acts at a distance to control expression throughout the genome. Genes Dev. *23*, 602–618.

Kelly, W.G., Schaner, C.E., Dernburg, A.F., Lee, M.H., Kim, S.K., Villeneuve, A.M., and Reinke, V. (2002). X-chromosome silencing in the germline of *C. elegans*. Development *129*, 479–492.

Kruesi, W.S., Core, L.J., Waters, C.T., Lis, J.T., and Meyer, B.J. (2013). Condensin controls recruitment of RNA polymerase II to achieve nematode X-chromosome dosage compensation. eLife *2*, e00808.

Langmead, B., and Salzberg, S.L. (2012). Fast gapped-read alignment with Bowtie 2. Nat. Methods *9*, 357–359.

Lau, A.C., Nabeshima, K., and Csankovszki, G. (2014). The *C. elegans* dosage compensation complex mediates interphase X chromosome compaction. Epigenet. Chromatin *7*, 31.

Le, T.B., and Laub, M.T. (2016). Transcription rate and transcript length drive formation of chromosomal interaction domain boundaries. EMBO J. *35*, 1582–1595.

Li, H., Handsaker, B., Wysoker, A., Fennell, T., Ruan, J., Homer, N., Marth, G., Abecasis, G., and Durbin, R.; 1000 Genome Project Data Processing Subgroup (2009). The Sequence Alignment/Map format and SAMtools. Bioinformatics *25*, 2078–2079.

Lin, K., Hsin, H., Libina, N., and Kenyon, C. (2001). Regulation of the *Caenorhabditis elegans* longevity protein DAF-16 by insulin/IGF-1 and germline signaling. Nat. Genet. *28*, 139–145.

Lo, T.W., Pickle, C.S., Lin, S., Ralston, E.J., Gurling, M., Schartner, C.M., Bian, Q., Doudna, J.A., and Meyer, B.J. (2013). Precise and heritable genome editing in evolutionarily diverse nematodes using TALENs and CRISPR/Cas9 to engineer insertions and deletions. Genetics *195*, 331–348.

Lupiáñez, D.G., Kraft, K., Heinrich, V., Krawitz, P., Brancati, F., Klopocki, E., Horn, D., Kayserili, H., Opitz, J.M., Laxova, R., et al. (2015). Disruptions of topological chromatin domains cause pathogenic rewiring of gene-enhancer interactions. Cell *161*, 1012–1025.

Martin, M. (2011). Cutadapt removes adapter sequences from high-throughput sequencing reads. EMBnet J. *17*, 10–12.

McDonel, P., Jans, J., Peterson, B.K., and Meyer, B.J. (2006). Clustered DNA motifs mark X chromosomes for repression by a dosage compensation complex. Nature *444*, 614–618.

Meyer, B.J. (2018). Sex and death: from cell fate specification to dynamic control of X-chromosome structure and gene expression. Mol. Biol. Cell *29*, 2616–2621.

Miller, L.M., Plenefisch, J.D., Casson, L.P., and Meyer, B.J. (1988). *xol-1*: a gene that controls the male modes of both sex determination and X chromosome dosage compensation in *C. elegans*. Cell *55*, 167–183.

Morales, C., and Losada, A. (2018). Establishing and dissolving cohesion during the vertebrate cell cycle. Curr. Opin. Cell Biol. *52*, 51–57.

Narendra, V., Rocha, P.P., An, D., Raviram, R., Skok, J.A., Mazzoni, E.O., and Reinberg, D. (2015). CTCF establishes discrete functional chromatin domains at the Hox clusters during differentiation. Science *347*, 1017–1021.

Nora, E.P., Goloborodko, A., Valton, A.L., Gibcus, J.H., Uebersohn, A., Abdennur, N., Dekker, J., Mirny, L.A., and Bruneau, B.G. (2017). Targeted degradation of CTCF decouples local insulation of chromosome domains from genomic compartmentalization. Cell *169*, 930–944.e22.

Nora, E.P., Lajoie, B.R., Schulz, E.G., Giorgetti, L., Okamoto, I., Servant, N., Piolot, T., van Berkum, N.L., Meisig, J., Sedat, J., et al. (2012). Spatial partitioning of the regulatory landscape of the X-inactivation centre. Nature *485*, 381–385.

Nusbaum, C., and Meyer, B.J. (1989). The Caenorhabditis elegans gene *sdc-2* controls sex determination and dosage compensation in XX animals. Genetics *122*, 579–593.

Oromendia, A.B., and Amon, A. (2014). Aneuploidy: implications for protein homeostasis and disease. Dis. Models Mech. *7*, 15–20.

Paul, M.R., Markowitz, T.E., Hochwagen, A., and Ercan, S. (2018). Condensin depletion causes genome decompaction Without altering the level of global gene expression in Saccharomyces cerevisiae. Genetics *210*, 331–344.

Pferdehirt, R.R., Kruesi, W.S., and Meyer, B.J. (2011). An MLL/COMPASS subunit functions in the *C. elegans* dosage compensation complex to target X chromosomes for transcriptional regulation of gene expression. Genes Dev. *25*, 499–515.

Pincus, Z., Smith-Vikos, T., and Slack, F.J. (2011). MicroRNA predictors of longevity in *Caenorhabditis elegans*. PLoS Genet. *7*, e1002306.

Podshivalova, K., Kerr, R.A., and Kenyon, C. (2017). How a mutation that slows aging can also disproportionately extend end-of-life decrepitude. Cell Rep. *19*, 441–450.

Ramírez, F., Ryan, D.P., Grüning, B., Bhardwaj, V., Kilpert, F., Richter, A.S., Heyne, S., Dündar, F., and Manke, T. (2016). deepTools2: a next generation web server for deep-sequencing data analysis. Nucleic Acids Res. *44*, W160–W165.

Rao, S.S.P., Huang, S.-C., Hilaire, B.G.S., Engreitz, J.M., Perez, E.M., Kieffer-Kwon, K.-R., Sanborn, A.L., Johnstone, S.E., Bascom, G.D., Bochkov, I.D., et al. (2017). Cohesin loss eliminates all loop domains. Cell *171*, 305–320.e24.

Rao, S.S.P., Huntley, M.H., Durand, N.C., Stamenova, E.K., Bochkov, I.D., Robinson, J.T., Sanborn, A.L., Machol, I., Omer, A.D., Lander, E.S., et al. (2014). A 3D map of the human genome at kilobase resolution reveals principles of chromatin looping. Cell *159*, 1665–1680.

Rhind, N.R., Miller, L.M., Kopczynski, J.B., and Meyer, B.J. (1995). *xo1-1* acts as an early switch in the *C. elegans* male/hermaphrodite decision. Cell *80*, 71–82.

Samuelson, A.V., Carr, C.E., and Ruvkun, G. (2007). Gene activities that mediate increased life span of *C. elegans* insulin-like signaling mutants. Genes Dev. *21*, 2976–2994.

Sanborn, A.L., Rao, S.S.P., Huang, S.C., Durand, N.C., Huntley, M.H., Jewett, A.I., Bochkov, I.D., Chinnappan, D., Cutkosky, A., Li, J., et al. (2015). Chromatin extrusion explains key features of loop and domain formation in wild-type and engineered genomes. Proc. Natl. Acad. Sci. USA *112*, E6456–E6465.

Schneider, C.A., Rasband, W.S., and Eliceiri, K.W. (2012). NIH Image to ImageJ: 25 years of image analysis. Nature Methods *9*, 671–675.

Schwarzer, W., Abdennur, N., Goloborodko, A., Pekowska, A., Fudenberg, G., Loe-Mie, Y., Fonseca, N.A., Huber, W., Haering, C.H., Mirny, L., et al. (2017). Two independent modes of chromatin organization revealed by cohesin removal. Nature *551*, 51–56.

Serizay, J., and Ahringer, J. (2018). Genome organization at different scales: nature, formation and function. Curr. Opin. Cell Biol. *52*, 145–153.

Snyder, M.J., Lau, A.C., Brouhard, E.A., Davis, M.B., Jiang, J., Sifuentes, M.H., and Csankovszki, G. (2016). Anchoring of heterochromatin to the nuclear lamina reinforces dosage compensation-mediated gene repression. PLoS Genet. *12*, e1006341.

Swierczek, N.A., Giles, A.C., Rankin, C.H., and Kerr, R.A. (2011). High-throughput behavioral analysis in *C. elegans*. Nat. Methods *8*, 592–598.

Swygert, S.G., Kim, S., Wu, X., Fu, T., Hsieh, T.H., Rando, O.J., Eisenman, R.N., Shendure, J., McKnight, J.N., and Tsukiyama, T. (2019). Condensin-dependent chromatin compaction represses transcription globally during quiescence. Mol. Cell *73*, 533–546.e4.

Taylor, R.C., and Dillin, A. (2013). XBP-1 is a cell-nonautonomous regulator of stress resistance and longevity. Cell *153*, 1435–1447.

Trapnell, C., Roberts, A., Goff, L., Pertea, G., Kim, D., Kelley, D.R., Pimentel, H., Salzberg, S.L., Rinn, J.L., and Pachter, L. (2012). Differential gene and transcript expression analysis of RNA-seq experiments with TopHat and Cufflinks. Nat. Protoc. *7*, 562–578.

Tzur, Y.B., Winter, E., Gao, J., Hashimshony, T., Yanai, I., and Colaiácovo, M.P. (2018). Spatiotemporal gene expression analysis of the *Caenorhabditis elegans* germline uncovers a syncytial expression switch. Genetics *210*, 587–605.

Valton, A.L., and Dekker, J. (2016). TAD disruption as oncogenic driver. Curr. Opin. Genet. Dev. *36*, 34–40.

Wang, X., Brandão, H.B., Le, T.B.K., Laub, M.T., and Rudner, D.Z. (2017). *Bacillus subtilis* SMC complexes juxtapose chromosome arms as they travel from origin to terminus. Science *355*, 524–527.

Wheeler, B.S., Anderson, E., Frøkjær-Jensen, C., Bian, Q., Jorgensen, E., and Meyer, B.J. (2016). Chromosome-wide mechanisms to decouple gene expression from gene dose during sex-chromosome evolution. eLife *5*, e17365.

Yonker, S.A., and Meyer, B.J. (2003). Recruitment of *C. elegans* dosage compensation proteins for gene-specific versus chromosome-wide repression. Development *130*, 6519–6532.

Yu, M., and Ren, B. (2017). The three-dimensional organization of mammalian genomes. Annu. Rev. Cell Dev. Biol. *33*, 265–289.

Zhang, Y., Liu, T., Meyer, C.A., Eeckhoute, J., Johnson, D.S., Bernstein, B.E., Nusbaum, C., Myers, R.M., Brown, M., Li, W., et al. (2008). Model-based analysis of ChIP-seq (MACS). Genome Biol. *9*, R137.

STAR★METHODS

KEY RESOURCES TABLE

REAGENT or RESOURCE	SOURCE	IDENTIFIER
Antibodies		
Rabbit polyclonal anti-DPY-27	Chuang et al., 1994	Rb699
Rabbit polyclonal anti-SDC-3	This paper	Rb3779
AffiniPure rabbit anti-rat IgG	Jackson ImmunoResearch Laboratories	Cat#312-005-003; AB_2339800
Alexa Fluor-488 AffiniPure IgG	Jackson ImmunoResearch Laboratories	Cat#111-545-003; AB_2338046
Bacterial and Virus Strains		
E. coli OP50	*Caenorhabditis* Genetics Center	OP50-1
E. coli HT115 (DE3)	*Caenorhabditis* Genetics Center	HT115(DE3)
E. coli HB101	*Caenorhabditis* Genetics Center	HB101
Chemicals, Peptides, and Recombinant Proteins		
Cas9-NLS purified protein	UC Berkeley QB3 MacroLab	N/A
Protein A Dynabeads	ThermoFisher Scientific	Cat#10002D
iQ SYBR Green Supermix	BioRad	Cat#170–8886
Cell-Tak	Corning	Cat#354240
Tunicamycin	Sigma-Aldrich	Cat#T7765; CAS: 11089-65-9
IPTG-Dioxane free	Denville Scientific	Cat#CI8280-4; CAS: 367-93-1
Paraquat Dichloride Hydrate	Millipore Sigma	Cat#36541; CAS: 75365-73-0
Deposited Data		
Hi-C, ChIP-seq, RNA-seq datasets	This paper	GEO: GSE128568
Experimental Models: Organisms/Strains		
C. elegans N2: Wild-type strain from Bristol	*Caenorhabditis* Genetics Center	Wild Type (WT)
C. elegans TY0810 grown on *sdc-2* RNAi bacteria: *sdc-2(y93, RNAi) X*	Nusbaum and Meyer, 1989	DCC mutant
C. elegans TY3936: *dpy-21(e428) V*	Yonker and Meyer, 2003	*dpy-21(null)*
C. elegans TY5648: *rex-32(y572) X*	Lo et al., 2013	*rex-32Δ*
C. elegans TY5815: *rex-47(y671) X*	Crane et al., 2015	*rex-47Δ*
C. elegans TY5826: *rex-32(y572) rex-33 (y743) X*	This paper	*2rexΔ*
C. elegans TY5818: *rex-14(y738) rex-47(y671) rex-8(y737) X*	This paper	*3rexΔ*
C. elegans TY5824: *rex-14(y738) rex-47(y671) rex-8(y737) rex-43(y741) rex-48(y742) rex35(y740) X*	This paper	*6rexΔ*
C. elegans TY5827: *rex-32(y572) rex-33(y743) rex-14(y738) rex-47(y671) rex-8(y737) rex-43(y741) rex-48(y742) rex-35(y740) X*	This paper	*8rexΔ*
C. elegans TY5910: *rex-32(y572) X*	This paper	*rex-32Δ*
C. elegans TY5911: *rex-33(y743) X*	This paper	*rex-33Δ*
C. elegans TY5755: *xol-1(y684) X*	This paper	*xol-1Δ*
C. elegans TY5828: *rex-32(y572) rex-33(y743) rex-14(y738) xol-1(y744) rex-47(y671) rex-8(y737) rex-43(y741) rex-48(y742) rex-35(y740) X*	This paper	*8rexΔ xol-1Δ*
C. elegans TY5868: *rex-32(y572) rex-33(y743) yIs197(rex-32) rex-14(y738) rex-47(y671) rex-8(y737) rex-43(y741) rex-48(y742) rex-35(y740) X*	This paper	*8rexΔ* plus *rex-32*

(*Continued on next page*)

Continued

REAGENT or RESOURCE	SOURCE	IDENTIFIER
C. elegans TY5872: *rex-32(y572) rex-33(y743) yIs197(rex-32) rex-14(y738) yIs201(rex-8) rex-47(y671) rex-8(y737) rex-43(y741) rex-48(y742) rex-35(y740) X*	This paper	*8rexΔ* plus *rex-32* & *rex-8*
C. elegans TY5854: *dpy-27(y679 FLAG) III; yIs187(rex-32) X*	This paper	*rex-32* insert
C. elegans TY5859: *yIs190(rex-47) I; rex-14(y738) rex-47(y671) rex-8(y737) X*	This paper	*3rexΔ* plus *rex-47* on Chr I
C. elegans TY5860: *yIs190(rex-47) yIs192(rex-8) I; rex-14(y738) rex-47(y671) rex-8(y737) X*	This paper	*3rexΔ* plus *rex-47* & *rex-8* on Chr I
C. elegans TY5867: *yIs196(rex-14) yIs190(rex-47) yIs192(rex-8) I; rex-14(y738) rex-47(y671)* rex-8(y737) X	This paper	*3rexΔ* plus *rex-14*, *rex-47* & *rex-8* on Chr I
Oligonucleotides		
CAGCGTAGTTGCTGACACTTAATGGTTC	This paper	chrX 15574551F
CTTTTAAGCAGTCGTCATGTACGTGTTCG	This paper	chrX 15574627R
CACTCCCCAGCTAATTTGGA	This paper	rex-32F
TTCCCTTGTTGCGGAGATAG	This paper	rex-32R
TTTATCCACCAACATGCATAAG	This paper	rex-8F
CAGTGGATAACTACACAAGGG	This paper	rex-8R
GTACAAACGCAGGGAAGAGA	This paper	rex-16F
GACGCTACCACACCTTCAATA	This paper	rex-16R
CTGCGCGATAGGCAATAGT	This paper	rex-48F
GCACAATTCCAAGTCATCCATAC	This paper	rex-48R
CCATATGTTGCCCAATGTTCC	This paper	rex-35F
CGCAGGGAACATCAAATTAGTC	This paper	rex-35R
Recombinant DNA		
RNAi plasmid for *C. elegans sdc-2*	Source BioScience	N/A
RNAi plasmid for *C. elegans daf-2*	Source BioScience	N/A
L4440 control plasmid for RNAi experiments	Source BioScience	RRID:Addgene_1654
Software and Algorithms		
hiclib	Imakaev et al., 2012	https://bitbucket.org/mirnylab/hiclib/
cworld	Job Dekker Lab	https://github.com/dekkerlab/cworld-dekker
cutadapt version 1.2.1	Martin, 2011	https://cutadapt.readthedocs.io/en/stable/
bowtie2 version 2.3.0	Langmead and Salzberg, 2012	http://bowtie-bio.sourceforge.net/bowtie2/index.shtml
SAMtools version 1.3.1	Li et al., 2009	http://www.htslib.org/
deepTools version 2.5.0.1	Ramírez et al., 2016	https://deeptools.readthedocs.io/en/develop/
ImageJ version 1.52j	Schneider et al., 2012	https://imagej.nih.gov/ij/
TopHat version 2.1.1	Trapnell et al., 2012	https://ccb.jhu.edu/software/tophat/index.shtml
Cufflinks version 2.2.1	Trapnell et al., 2012	https://github.com/cole-trapnell-lab/cufflinks
cummeRbund version 2.20.0	Trapnell et al., 2012	http://compbio.mit.edu/cummeRbund/
Prism7	GraphPad	https://www.graphpad.com/scientific-software/prism/
Choreography	Swierczek et al., 2011	https://github.com/lchoran/choreography

LEAD CONTACT AND MATERIALS AVAILABILITY

Further information and requests for reagents may be directed to and will be fulfilled by the Lead Contact, Barbara J. Meyer (bjmeyer@berkeley.edu).

EXPERIMENTAL MODEL AND SUBJECT DETAILS

C. elegans Strains

C. elegans strains were grown at 20°C on either NGM plates with HB101 bacteria, NGM plates with OP50 bacteria, or RNAi plates (NGM agar with 1 mM IPTG and 100 μg/mL carbenicillin) with HT115 bacteria carrying an RNAi plasmid (*sdc-2* or pL4440 negative control). Bacteria were grown as in (Crane et al., 2015). To collect embryos, starved L1s were plated on bacteria and grown at 20°C for three days. The gravid adults were then bleached to isolate mixed-stage embryos. When *sdc-2(y93)* worms (Nusbaum and Meyer, 1989) were grown on RNAi bacteria from the L1 stage, their progeny died as embryos or L1s.

Experiments measuring thermotolerance, sensitivity to mitochondrial stress, or lifespan required the use of staged worms. To stage worms, gravid adults were bleached to release embryos using a solution of 1.8% sodium hypochlorite and 0.375 M KOH. Progeny were grown for 12–16 hr without food in M9 buffer (22 mM KH_2PO_4 monobasic, 42.3 mM Na_2HPO_4, 85.6 mM NaCl, 1mM $MgSO_4$) until they developed into arrested L1 larvae.

METHOD DETAILS

rex Deletions and Insertions

rex-32 and *rex-47* deletions were previously published (Crane et al., 2015; Lo et al., 2013). All other *rex* deletions and insertions were made using CRISPR/Cas9. To generate the *6rexΔ* strain, the right six *rex* sites at DCC-dependent boundaries were deleted sequentially, and the resulting strain was outcrossed four times using TY0456 *dpy-6(e14) unc-3(e151) X*. To generate the *rex-32Δ rex-33Δ* strain, *rex-33* was deleted in TY5648, which carried a *rex-32* deletion, and the strain was outcrossed three times using *lon-2(e678) X*. To build the *8rexΔ* strain, *6rexΔ* was crossed to the *rex-32Δ rex-33Δ* strain and recombinant F2s with all eight *rex* deletions were selected. The *rex-32Δ* and *rex-33Δ* strains (TY5910 and TY5911, respectively) used for lifespan experiments were created by crossing *rex-32Δ rex-33Δ* (TY5826) to wild-type males and selecting recombinant F2s with single deletions. All other strains used for Hi-C experiments were outcrossed at least two times.

For the *rex-14*, *rex-8*, *rex-43*, *rex-48*, and *rex-35* deletions, worms were injected with plasmids encoding Cas9 and the sgRNA along with either a plasmid or oligo repair template as in (Farboud and Meyer, 2015). Repair templates consisted of a 6 bp NcoI restriction site flanked by homology arms (500-1000 bp for plasmids or at least 50 bp for oligos). Each deletion replaced the *rex* site with a 6 bp NcoI restriction site to facilitate screening for deletions. The *rex-33* deletion was made using a Cas9 RNP along with an oligo repair template (Farboud et al., 2019), and all *rex* site insertions were made as in (Farboud et al., 2019) using the Cas9 RNP, gBlocks (IDT) with ~200 bp homology arms as repair templates, and either *dpy-10* or *rol-6* co-conversion markers. The locations and sizes of insertions and deletions and guide RNA sequences are listed in Table S1.

Hi-C and Analysis

Wild-type and *rex* site deletion and insertion worms were grown on NGM plates with HB101 bacteria, and *sdc-2(y93)* worms were grown on RNAi plates with HT115 bacteria carrying an *sdc-2* (RNAi) plasmid. *In situ* Hi-C was performed on nuclei isolated from mixed stage embryos and data were processed as in (Brejc et al., 2017). Hi-C was performed for two biological replicates of wild type, TY5815 *rex-47Δ*, TY5824 *6rexΔ*, TY5827 *8rexΔ*, and TY0810 DCC mutant and a single replicate for TY5818 *3rexΔ*, TY5868 *8rexΔ plus rex-32*, TY5872 *8rexΔ plus rex-32 & rex-8*, TY5854 *rex-32* insert, TY5859 *3rexΔ* plus *rex-47* on I, TY5860 *3rexΔ* plus *rex-47 & rex-8* on I, and TY5867 *3rexΔ* plus *rex-14, rex-47 & rex-8* on I. Z-score subtraction heatmaps and insulation plots were generated by comparing single Hi-C replicates of each genotype. Patterns of boundary loss and gain were completely reproducible between replicates. For strains with two replicates, interaction frequencies after iterative correction from the two replicates were combined. Boundary pileups in Figure 2I, 3D plots, and scaling plots were generated using the combined replicates. Average interaction frequencies at increasing distances in Figures 4D–4G were calculated using fragment-level (unbinned) contacts using the *hiclib* library for Python (https://bitbucket.org/mirnylab/hiclib) (Imakaev et al., 2012).

To assess how removing a boundary affects the strength of adjacent boundaries (Figure 2I), data from *rex-47Δ*, *3rexΔ*, *6rexΔ*, and *8rexΔ* X chromosomes were used to calculate the average insulation profile around all boundaries adjacent to a deleted boundary and the average insulation profile at the same boundaries in the strain with the next fewer deletions. For example, the boundary upstream of *rex-14* in *3rexΔ* was compared to the same boundary in *rex-47Δ*. Two replicates for each of 12 boundaries were included for 24 total comparisons. Similar analysis was performed for the seven boundaries that are two boundaries away from deleted boundaries for 14 total comparisons. The insulation scores at the boundaries were used to calculate a p value using a paired t test.

ChIP-seq

Wild-type, *8rexΔ*, TY5872 *8rexΔ* plus *rex-32* & *rex-8*, and TY5867 *3rexΔ* plus *rex-14*, *rex-8* & *rex-47* on I strains were grown on RNAi plates with HT115 bacteria carrying the empty plasmid vector pL4440. Approximately 0.5 g of mixed-stage embryos were isolated as above and frozen in liquid nitrogen. Embryos were washed once in 2% formaldehyde in M9 buffer and then fixed for 30 min with gentle rocking in 50 mL 2% formaldehyde in M9 buffer. Embryos were washed in 10mM Tris-HCl (pH 7.5) and then in FA buffer (150 mM NaCl, 50 mM HEPES-KOH pH 7.6, 1 mM EDTA, 1% Triton X-100, 0.1% sodium deoxycholate) and resuspended in FA buffer with protease inhibitors (5 mM DTT, protease inhibitor cocktail, 1 mM PMSF) to a total volume of 1 mL. Embryos were ground with 50 strokes in a 2 mL dounce homogenizer. Sarkosyl was added to a final concentration of 0.1% and chromatin was sheared in an

S2 Covaris with duty cycle 20%, intensity 8, and 200 cycles/burst for 30 cycles of 60 sec with 45 sec of rest for a total time of 52 min. The extract was centrifuged at maximum speed for 15 min at 4°C. Supernatant containing approximately 2 mg total protein was incubated with 6.6 μg rabbit polyclonal anti-DPY-27 antibody (Rb699) (Chuang et al., 1994), rabbit polyclonal anti-SDC-3 antibody (Rb3779) directed to amino acids 1,068–1,342, or random IgG antibodies overnight at 4°C in a volume of at least 500 μl. 50 μl of Protein A Dynabeads (ThermoFisher Scientific, 10002D) were washed in FA buffer three times, added to the immunoprecipitation, and mixed at 4°C for at least 2 hr. Beads were then washed, DNA eluted, and libraries prepared as in (Kruesi et al., 2013). Libraries were sequenced with 50 bp single-end reads on an Illumina HiSeq4000 platform.

ChIP-seq Analysis

Adapters were trimmed using cutadapt version 1.2.1 (Martin, 2011), and reads were then aligned to the ce11 genome using bowtie2 version 2.3.0 (Langmead and Salzberg, 2012) with default settings. For comparisons involving strains with *rex* site insertions, the reference genome was modified to incorporate the *rex* insertions. Reads were sorted using SAMtools version 1.3.1 (Li et al., 2009), and read coverage was calculated by normalizing the read number in each 50 bp bin to the total read number using the bamCoverage function in deepTools version 2.5.0.1 (Ramírez et al., 2016) with the "normalizeUsingRPKM" option. Analysis of data from wild-type and *8rexΔ* strains was performed with two combined biological replicates, and one replicate was used for data from TY5872 *8rexΔ* plus *rex-32* & *rex-8* and TY5867 *3rexΔ* plus *rex-14*, *rex-8* & *rex-47* strains.

To calculate the number of reads mapping to each *rex* site, SDC-3 peaks were first identified using macs2 version 2.1.1 (Zhang et al., 2008) with IgG as the control and the mfold parameter set to 3 50. The total SDC-3 reads in a 400 bp window surrounding each peak were summed and the IgG reads in the same window were subtracted. The peaks were then ranked based on this read number and the strongest 30 peaks (which were all on chromosome X) were used for analyses (*rex-48*, *rex-8*, *rex-23*, *rex-14*, *rex-32*, *rex-33*, *rex-43*, *rex-35*, *rex-16*, *rex-40*, *Prex-30*, *rex-45*, *rex-47*, *rex-34*, *Prex-7*, *rex-41*, *Prex-22*, *rex-6*, *rex-2*, *Prex-31*, *rex-24*, *rex-44*, *rex-36*, *Prex-6*, *rex-1*, *rex-42*, *Prex-1*, *rex-46*, *rex-39*).

To quantify DCC binding at inserted *rex* sites, reads were mapped to reference genomes modified to include the insertions (and deletions of the endogenous sites). Reads were summed in a 400 bp window around the peak of the inserted *rex* site as well as around four strong *rex* sites on X (*rex-40*, *rex-23*, *rex-16*, and *Prex-30*). Binding was normalized by dividing binding at the inserted *rex* site by the average binding at the other four *rex* sites.

The bigwigCompare function in deepTools version 2.5.0.1 (Ramírez et al., 2016) was used to calculate the $\log_2$ ratio of DCC binding between genotypes, and the median ratio in a 1 kb sliding window was plotted. Ratios were not calculated for the basepairs in the deletions or insertions.

ChIP-qPCR

ChIP-qPCR was used to quantify DCC binding at *rex-32* inserted in the wild-type background. The *rex-32* insert strain (TY5854) was grown on MYOB plates with HB101 bacteria. ChIP using anti-SDC-3 antibody was performed on three biological replicates of mixed-stage TY5854 embryos as described above. After elution, DNA was diluted 4-fold and qPCR was performed using SYBR green (BioRad iQ SYBR Green Supermix 170–8886) on a BioRad CFX384 Real-Time System. The oligos used to measure binding 50 bp from the *rex-32* insertion, at the endogenous *rex-32* site, and at other strong *rex* sites for normalization (*rex-8*, *rex-16*, *rex-48*, and *rex-35*) are listed in the Key Resources Table.

Standard curves were generated using input DNA, and binding at each *rex* site was calculated as a percentage of input. Binding at the inserted *rex-32* in Figure S4B was normalized to the average binding at five strong *rex* sites (*rex-32*, *rex-8*, *rex-16*, *rex-48*, and *rex-35*).

Measuring X Chromosome Volume

Intestines of adults (2 days post-L4) grown on OP50 bacteria were stained with anti-DPY-27 antibody (rb699) (Chuang et al., 1994) and DAPI, confocal images were scanned and deconvolved, and X chromosome volume was calculated as in (Brejc et al., 2017).

Measurements of X Chromosome Nuclear Position

To measure the position of X chromosomes within the nucleus, X chromosomes were visualized in wild-type and *8rexΔ* embryos using indirect immunofluorescence for the DCC component DPY-27. The proportion of the chromosome located in each of three concentric zones of equal area was calculated as in (Snyder et al., 2016). Embryos at the ~120-150-cell stage were stained as in (Brejc et al., 2017) using rabbit polyclonal anti-DPY-27 (rb699) (Chuang et al., 1994) and Alexa Fluor-488 goat anti-rabbit antibodies (Jackson Immunoresearch Laboratories, Inc). Images were acquired and deconvolved as in (Brejc et al., 2017) with 50 nm XY pixel size and 80 nm Z step size. For each embryo, 0.4 μm Z projections were made by summing five Z slices. For each nucleus, the projection with the highest total DPY-27 signal was selected, and a circular or oval region of interest was drawn by hand around the nucleus in ImageJ. The average DPY-27 signal in a cytoplasmic region was calculated, and this background value was subtracted from the nuclear DPY-27 signal. The nucleus was divided into three concentric ovals of equal areas. The total DPY-27 signal (after background subtraction) in each zone was calculated using ImageJ. The average percentage of X signal located in each of the three zones and the standard error of the mean were plotted for 41 wild-type nuclei from four embryos and 45 *8rexΔ* nuclei from four embryos.

RNA-seq Library Preparation and Analysis

For each RNA-seq replicate, worms were grown, embryos collected, and RNA-seq performed for all genotypes in parallel. Worms were grown on RNAi plates with HT115 bacteria with either *sdc-2* RNAi (for DCC mutant) or pL4440 empty vector (for wild type and *8rex⊿*). For some replicates, mixed-stage embryos (majority pre-comma stage) were isolated by bleaching gravid hermaphrodites as above. Other replicates were skewed towards older embryos by bleaching young adults (68–70 hr after plating starved L1s) to isolate young embryos, letting the embryos develop at 20°C for 7–8 hr until the majority were at the three-fold stage, and then freezing. RNA was isolated and RNA-seq libraries were prepared as in (Brejc et al., 2017), and libraries were sequenced with 50 bp reads on an Illumina HiSeq4000 platform. Reads were processed by trimming adapters using cutadapt version 1.2.1, aligning to the ce11 reference genome using TopHat version 2.1.1, and assembling using Cufflinks version 2.2.1 (Trapnell et al., 2012).

The wild-type and *8rex⊿* replicates that were most closely stage-matched were computationally identified. A published dataset that measured gene expression in single embryos through embryogenesis (whole embryo time course from (Hashimshony et al., 2015)) was used to select autosomal genes that had at least 1 transcript per million at some point in the time course and had at least a 20-fold change from their lowest to highest expression level. The expression levels for each of these 12,750 genes were scaled by subtracting the gene's mean expression and dividing by its standard deviation. The genes were k-means clustered into five clusters with similar temporal expression patterns using the kmeans function in R (Figure S5D). For each paired replicate of wild-type and *8rex⊿* RNA-seq data, expression of genes in each of the five clusters was compared between genotypes, and the five replicates in which the two genotypes had similar expression levels for genes in each cluster were selected. Two replicates of mixed-stage embryos and three replicates of late embryos were included, and other replicates in which the wild-type embryos clearly had higher expression of late genes and lower expression of early genes compared to *8rex⊿* were excluded. For the *sdc-2(y93, RNAi)* to wild-type comparison, two replicates of mixed-stage embryos and one replicate of older embryos were used.

Replicates were combined using Cuffmerge. Expression levels (fpkm) and fold changes were analyzed using cummeRbund version 2.20.0. The p values comparing X to autosomal expression were calculated for genes with greater than 1 FPKM using a two-sided Wilcoxon rank-sum test.

xol-1 Rescue

A 3,035 bp deletion of the *xol-1* open reading frame (X:8041318-8043793) was made in the *rex* deletion background using Cas9 with two sgRNAs (GCTTCAACCTGCATTTCTGG and TGATTGATATGGGAAATGG). Ten *8rex⊿ xol-1⊿* hermaphrodites were crossed to wild-type males, and all cross progeny were either healthy hermaphrodites or inviable embryos, the phenotype of *xol-1* mutant XO animals. No viable male F1s were observed in the ten broods (approximately 3000 progeny), indicating that *8rex⊿* does not rescue *xol-1⊿* males.

Imaging the Timing of Embryogenesis

To measure the timing of embryogenesis in wild-type and *8rex⊿* strains, embryos of both genotypes were imaged simultaneously. 3.5 μL of a 1:10 dilution of Cell-Tak (Corning, catalog # 354240) and 1.8 μL of 1 N NaOH were combined, and 3 μL were pipetted onto a coverslip. After the coverslips dried, 2 μL of poly-L-lysine solution were added and allowed to dry, and coverslips were rinsed with ethanol and then water. Two-cell embryos of the first genotype in M9 buffer were transferred onto the Cell-Tak spot on the coverslip and aligned using an eyebrow hair. After the embryos settled, the coverslip was rinsed with M9 and imaged to document the positions of embryos. Two-cell embryos of the second genotype were then placed on a 2% agarose pad. The coverslip having embryos of the first genotype was then placed on the agarose pad having embryos of the second genotype and sealed with rubber cement. Each embryo was imaged every 3 min for 13 hr using the Mark and Find function on a Leica SP8 WLL confocal microscope with a 20× objective in a room that was 22-23°C. The image of the coverslip with the embryos of the first genotype was used to identify the genotypes of all embryos. The times when each embryo reached comma stage, completed two-fold stage, and hatched were determined. A total of 19 embryos of each genotype were imaged over three separate days.

Thermotolerance

For each genotype, starved L1 larvae were grown to day 1 of adulthood on RNAi plates with HT115 bacteria. Ten day 1 adults were then placed on each of five RNAi plates with HT115 bacteria. The plates were incubated at 37°C, and the number of living and dead worms were counted after 5, 7, and 9 hr. Any worms that crawled onto the sides of the plates were censored. Generally, at 5 hr, most worms were still alive, and by 9 hr, nearly all were dead. The percentage of worms alive at 7 hr was reported for eleven replicates of wild-type and *8rex⊿* animals performed on separate days and six replicates of *2rex⊿* and *6rex⊿* animals. In four additional replicates, the percentage alive was reported at 5, 6, or 9.5 h to accommodate slight variability in timing of demise due to heat stress (Table S4). P values were calculated using a paired two-tailed t test.

Sensitivity to Mitochondrial Stress

Starved L1 wild-type, *8rex⊿*, *2rex⊿*, and *6rex⊿* worms were grown to day 1 of adulthood at 20°C (three days) on RNAi plates with HT115 bacteria carrying an empty vector (pL4440). Wild-type worms were also grown on HT115 bacteria carrying *daf-2*(RNAi) plasmid as a positive control for increased resistance to oxidative stress. For each condition, five adult day 1 hermaphrodites were placed in each of 12 wells containing 50 μL of freshly prepared 0.2 M paraquat dichloride hydrate (Millipore Sigma 36541) in S-basal media (0.1 M NaCl, 0.05 M potassium phosphate pH 6, 5 μg/mL cholesterol), for a total of 60 worms. Worms were incubated

at 20°C in a dark box. Every 2 hr, the number of surviving worms was scored by observing each worm for movement (thrashing, pharyngeal pumping, etc.) for 15-20 sec. Results were averaged from three replicates for *8rexΔ*, *2rexΔ*, and *6rexΔ*, four replicates for *daf-2(RNAi)*, and five replicates for wild type. Error bars show standard error of the mean.

Lifespan Analysis

For lifespan experiments, starved L1s were grown at 20°C on RNAi plates with HT115 bacteria carrying empty vector (pL4440). Starting at day 1 of adulthood until the animals stopped laying embryos (day 7-9), the worms were transferred daily to fresh plates away from their progeny. The number of living and dead worms were then counted every two days. Worms that crawled off the plate or exhibited an exploded gonad or internal hatching of progeny were censored from the experiment. For all lifespan studies, worms were grown at 20°C in a dark box, and the experimenter was blind to the animals' genotypes. Statistical analysis was performed using Prism 6 software.

For male lifespan analysis, each day 1 adult male was placed on an individual plate and scored every two days. The majority of males crawled off the plate before dying and were censored.

Hermaphrodite sensitivity to ER stress was assayed by measuring survival in the presence of tunicamycin. Wild-type, *8rexΔ*, *6rexΔ*, and *2rexΔ* starved L1 larvae were grown to day 1 of adulthood on RNAi plates with HT115 bacteria carrying empty vector plasmid pL4440. Day 1 adults were moved to RNAi plates with either 1% DMSO (control) or 20 ng/μL tunicamycin, and their lifespans were assayed.

Worm Tracking

Worm movement was measured using a Multi-Worm Tracker as in (Podshivalova et al., 2017). Briefly, animals were grown on OP50 bacteria, and 50 μM 5-fluoro-2'-deoxyuridine (FUDR) was added to the plates when animals reached the late L4 stage to prevent progeny from developing. Tracking was performed daily or every other day for 1260 sec with a tap stimulus delivered after 900 sec. Explorative locomotion was measured over a 50 sec time window after allowing animals to recover from handling for 650 sec. Stimulated movement was measured over a 1 sec time window following the delivery of a single tap stimulus using a solenoid plate tapper. Animals that moved by less than half a body length within a 1 min time interval were not detected. After detection, tracking continued even if the animal was still. For each genotype, eight plates each with 50 worms were tracked on eight parallel trackers. Animals that had exploded or would otherwise be censored during analysis of lifespan were removed from plates prior to tracking. Data analysis was performed using Choreography software (Swierczek et al., 2011).

QUANTIFICATION AND STATISTICAL ANALYSIS

All quantification and statistical analyses are explained in the relevant sections of the STAR Methods. Statistics are presented in the text and figure legends.

DATA AND CODE AVAILABILITY

The acession number for the Hi-C, ChIP-seq, and RNA-seq raw and processed data reported in this paper is GEO: GSE128568.

Developmental Cell, Volume *51*

Supplemental Information

X Chromosome Domain Architecture Regulates *Caenorhabditis elegans* Lifespan but Not Dosage Compensation

Erika C. Anderson, Phillip A. Frankino, Ryo Higuchi-Sanabria, Qiming Yang, Qian Bian, Katie Podshivalova, Aram Shin, Cynthia Kenyon, Andrew Dillin, and Barbara J. Meyer

Figure S1

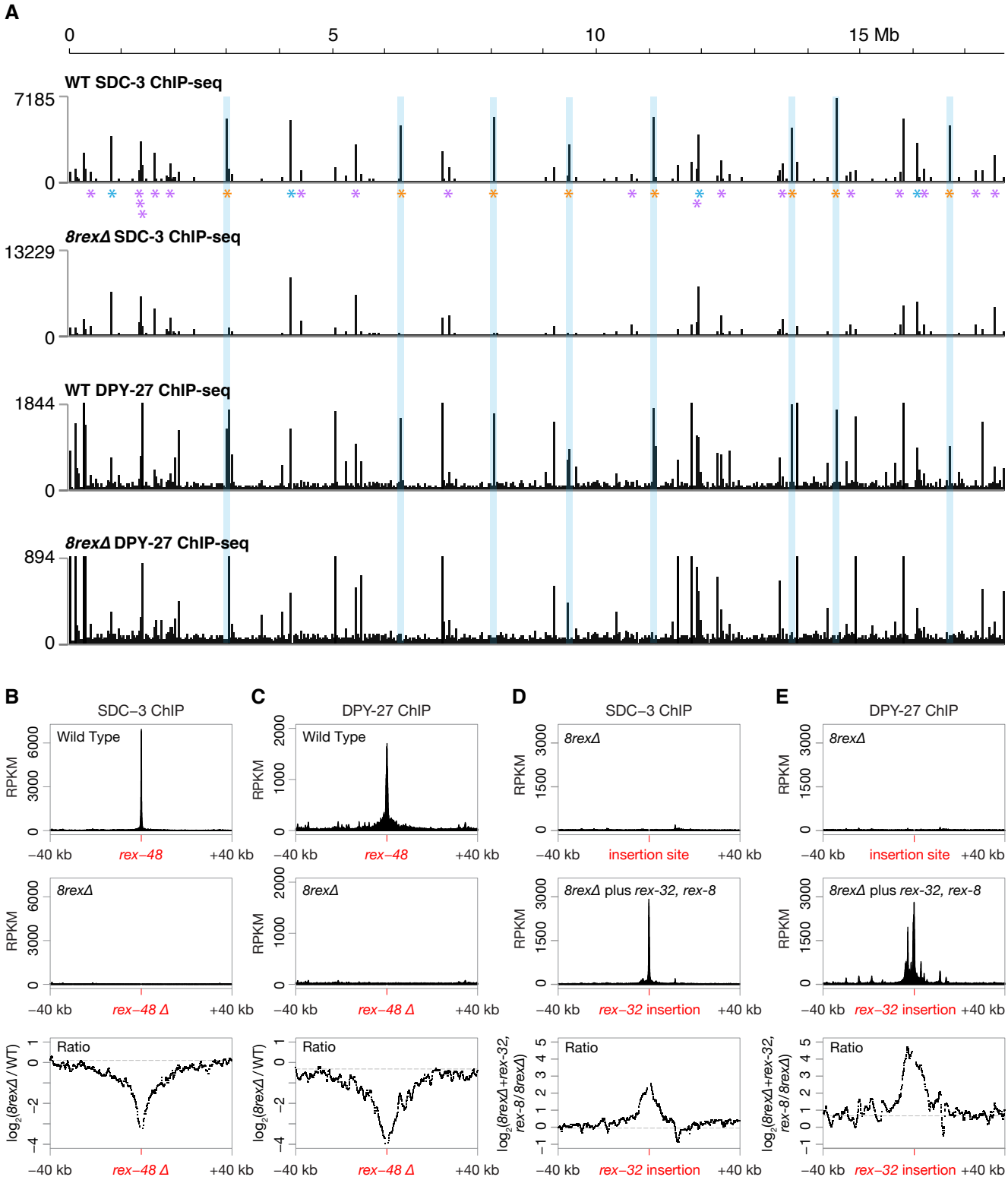
A
0
5
10
15 Mb
WT SDC-3 ChIP-seq
7185
0
8rexΔ SDC-3 ChIP-seq
13229
0
WT DPY-27 ChIP-seq
1844
0
8rexΔ DPY-27 ChIP-seq
894
0
B
SDC–3 ChIP
Wild Type
8rexΔ
RPKM
−40 kb
rex–48
rex–48 Δ
+40 kb
Ratio
log2(8rexΔ / WT)
C
DPY-27 ChIP
D
SDC–3 ChIP
8rexΔ plus rex-32, rex-8
insertion site
rex–32 insertion
log2(8rexΔ+rex-32, rex-8/8rexΔ)
E
DPY-27 ChIP

Figure S1. DCC Binding at Deleted *rex* Sites Is Abolished But Most DCC Binding on X Persists, Related to Figure 1

(A) SDC-3 and DPY-27 ChIP-seq profiles on X chromosomes of wild-type and *8rexΔ* embryos. Plots are scaled based on the binding at four strong *rex* sites that were not deleted (*rex-40*, *rex-23*, *rex-16*, and *Prex-30*, blue asterisks left to right, respectively). Other *rex* sites that were not deleted are marked with purple asterisks. Blue stripes and orange asterisks highlight the locations of the eight deleted *rex* sites.

(B and C) SDC-3 and DPY-27 ChIP-seq RPKM (reads per kilobase of transcript per million mapped reads) in the 80 kb region surrounding *rex-48* in wild-type embryos (top) and surrounding the *rex-48* deletion in *8rexΔ* embryos (middle). Red ticks show the location of the 408 bp *rex-48* deletion. Bottom plots display the $\log_2$ ratio of ChIP-seq reads in *8rexΔ* versus wild-type embryos. Ratios were not calculated for the deleted region. Gray dashed lines show the median ratio of signal between genotypes for the entire X chromosome. Binding of SDC-3 and DPY-27 was reduced immediately adjacent to the deletions but returned to wild-type levels within 20 kb.

(D and E) SDC-3 and DPY-27 ChIP-seq RPKM in the 80 kb region surrounding the location of the inserted *rex-32* in *8rexΔ* and in *8rexΔ* plus *rex-32*, *rex-8* embryos. Red ticks show the location of the 592 bp *rex-32* insertion. As above, bottom plots show the $\log_2$ ratio of DCC binding between genotypes. Binding of SDC-3 and DPY-27 was increased immediately adjacent to the insertions but returned to wild-type levels within 15 kb.

Figure S2

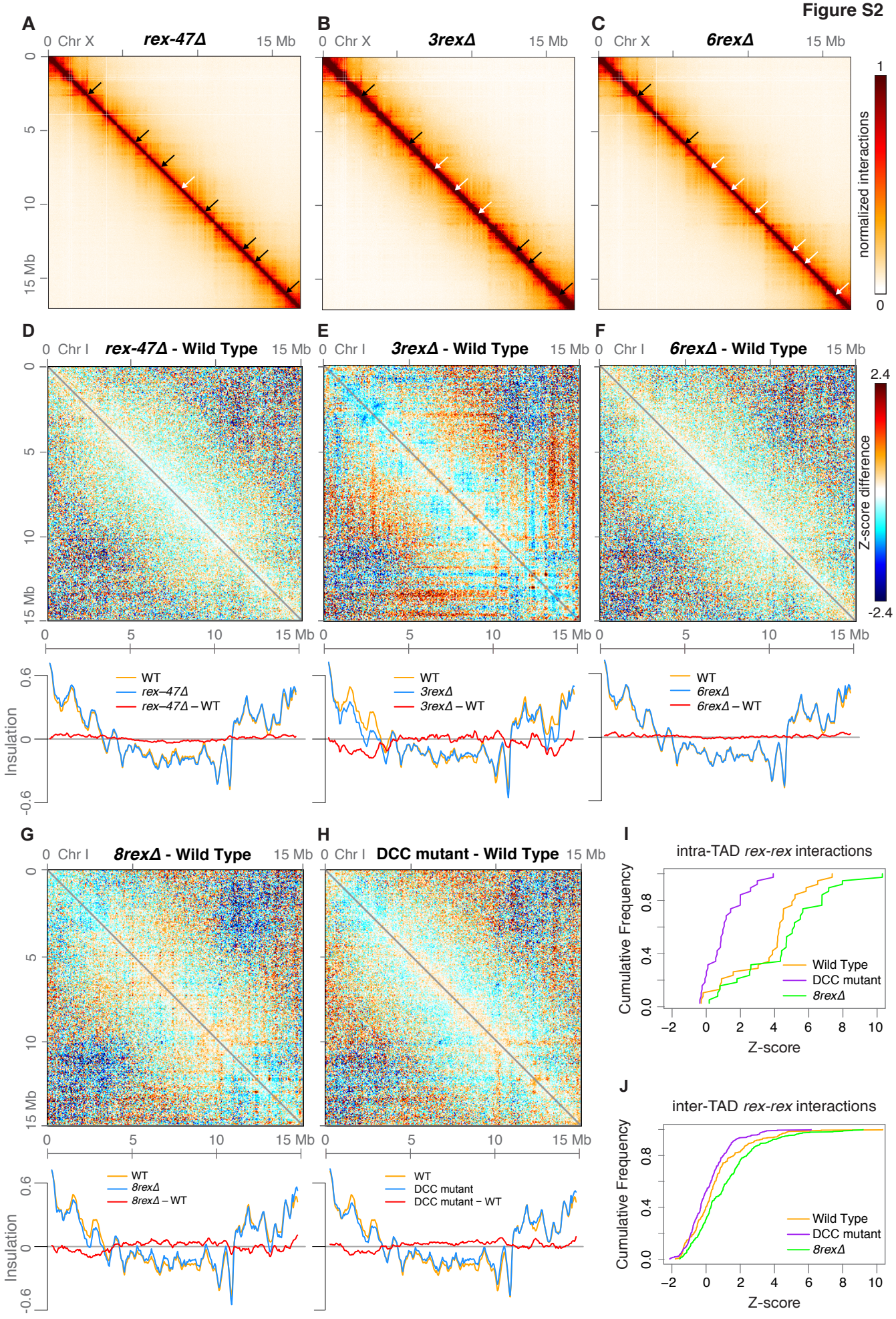
A
rex-47Δ
B
3rexΔ
C
6rexΔ
0 Chr X
15 Mb
normalized interactions
1
0
D
rex-47Δ - Wild Type
E
3rexΔ - Wild Type
F
6rexΔ - Wild Type
0 Chr I
Z-score difference
2.4
-2.4
WT
rex–47Δ
rex–47Δ – WT
3rexΔ
3rexΔ – WT
6rexΔ
6rexΔ – WT
Insulation
G
8rexΔ - Wild Type
H
DCC mutant - Wild Type
8rexΔ
8rexΔ – WT
DCC mutant
DCC mutant – WT
I
intra-TAD rex-rex interactions
Cumulative Frequency
Z-score
Wild Type
DCC mutant
8rexΔ
J
inter-TAD rex-rex interactions

Figure S2. *rex* Deletions Cause X-Specific Changes in Chromosome Structure, Related to Figure 1

(A-C) X chromosome heatmaps binned at 20 kb show Hi-C interactions in *rex-47Δ*, *3rexΔ*, and *6rexΔ* embryos. White arrows mark the positions of deleted *rex* sites, and black arrows mark remaining DCC-dependent boundaries.

(D-H) Z-score subtraction heatmaps of chromosome I binned at 50 kb show increased (red) and decreased (blue) Hi-C interactions in four strains with different numbers of *rex* deletions and in a DCC mutant strain [*sdc-2(y93, RNAi)*] compared to the wild-type strain. Lower plots show insulation scores across chromosome I in *rex* deletion or DCC mutant (blue) and in wild-type (orange) strains and the insulation score difference between genotypes (red).

(I and J) Cumulative frequency of interaction Z-scores for interactions between *rex* sites within the same TAD (I) or between *rex* sites in separate TADs (J). In *8rexΔ* embryos, higher interactions occur between *rex* sites located across deleted boundaries and between *rex* sites within regions defined as TADs on the wild-type X. Only the 22 non-boundary *rex* sites with the highest SDC-3 binding were analyzed, and only interactions between sites within 4 Mb were included.

Figure S3

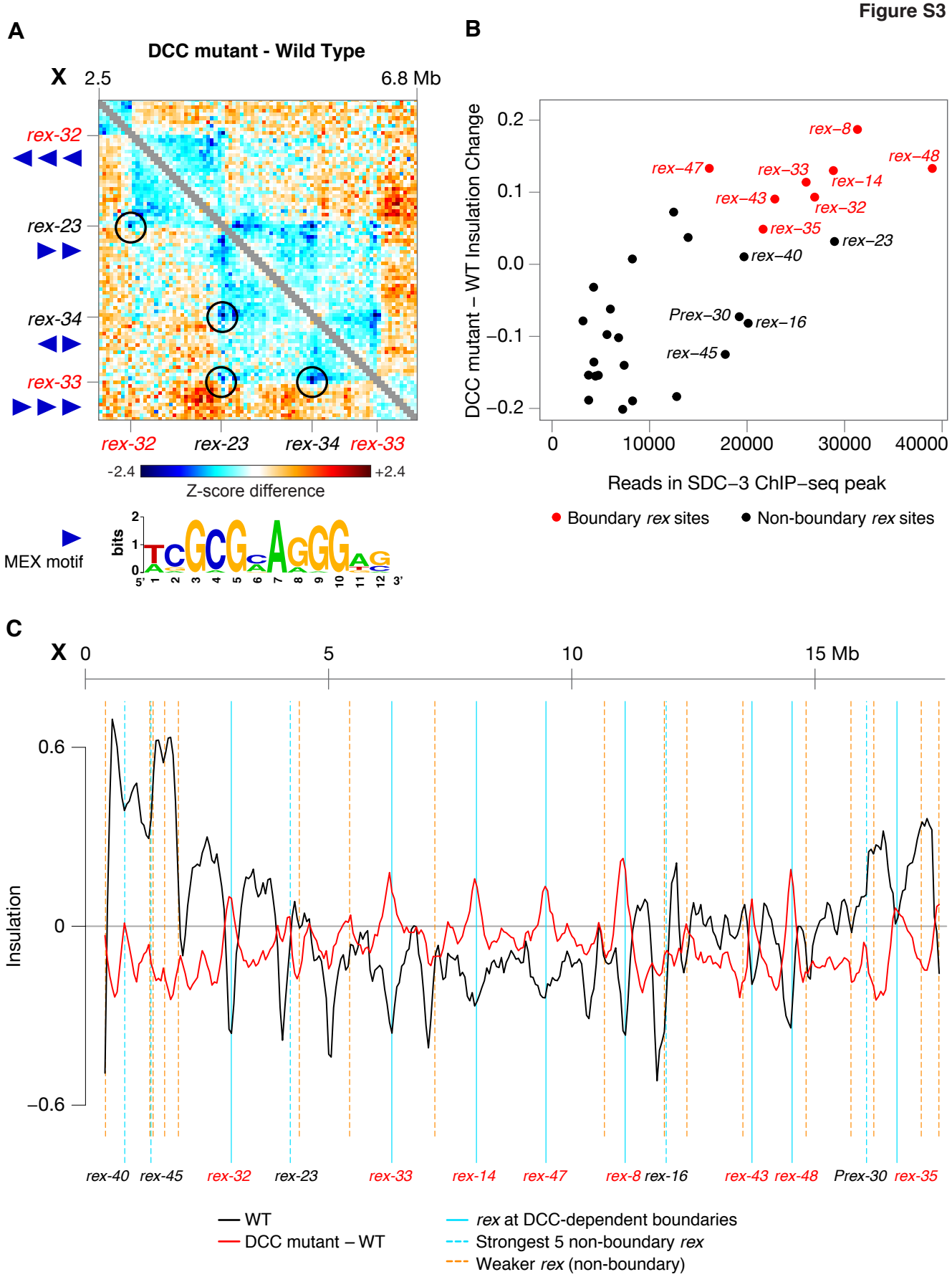
A
DCC mutant - Wild Type
X 2.5 6.8 Mb
rex-32
rex-23
rex-34
rex-33
-2.4 +2.4
Z-score difference
MEX motif
bits
B
DCC mutant – WT Insulation Change
Reads in SDC–3 ChIP–seq peak
Boundary rex sites
Non-boundary rex sites
C
X 0 5 10 15 Mb
Insulation
WT
DCC mutant – WT
rex at DCC-dependent boundaries
Strongest 5 non-boundary rex
Weaker rex (non-boundary)

Figure S3. Only High-Occupancy *rex* Sites Establish TAD Boundaries, Related to Figure 1
(A) Examples showing that *rex* sites interact regardless of the orientation in these sites of known X-enriched motifs (MEX) important for DCC binding. Z-score subtraction heatmap of a portion of the X chromosome shows increased (red) and decreased (blue) interactions in DCC mutant versus wild-type embryos. Circles mark DCC-dependent interactions among four *rex* sites. Loss of a specific interaction in DCC mutants is reflected in a blue corner peak. For each *rex* site, blue triangles show the orientations of MEX motifs with a score less than -12 (Jans et al., 2009). *rex-23* (plus strand motifs) interacts with sites that have minus strand motifs (*rex-32*), plus strand motifs (*rex-33*), or both (*rex-34*). *rex-34* (both orientations) also interacts with *rex-23* (plus strand motifs).
(B) Correlation between insulation score change and DCC binding. For each of the 30 highest-occupancy *rex* sites, the insulation score difference in DCC mutant versus wild-type strains is plotted against the level of SDC-3 binding. SDC-3 levels were calculated by summing ChIP-seq reads mapping within 200 bp of the summit. *rex* sites at DCC-dependent boundaries are colored red. Five *rex* sites have more binding than *rex-47* but do not create boundaries (*rex-23*, *rex-16*, *rex-40*, *Prex-30*, and *rex-45*).
(C) Insulation profile of X chromosomes in the wild-type strain and insulation profile difference between wild-type and DCC mutant strains. Insulation scores were calculated by summing interactions in a 250 kb sliding window. (Plots in all other figures used a 500-kb window.) All DCC-dependent boundaries (solid cyan lines) contain one of the 13 highest-occupancy *rex* sites. Five *rex* sites that have the same or more DCC binding as boundary *rex* sites (dotted cyan lines) are not at boundaries (not at local minima in the wild-type insulation profile, black line) but do show insulation changes in the DCC mutant (local maxima in the insulation profile difference, red line). That is, in DCC mutants, interactions between loci flanking these non-boundary *rex* sites increased compared to interactions across neighboring loci. Insulation score changes also occur at some *rex* sites of rank 14-30 (dotted orange lines).

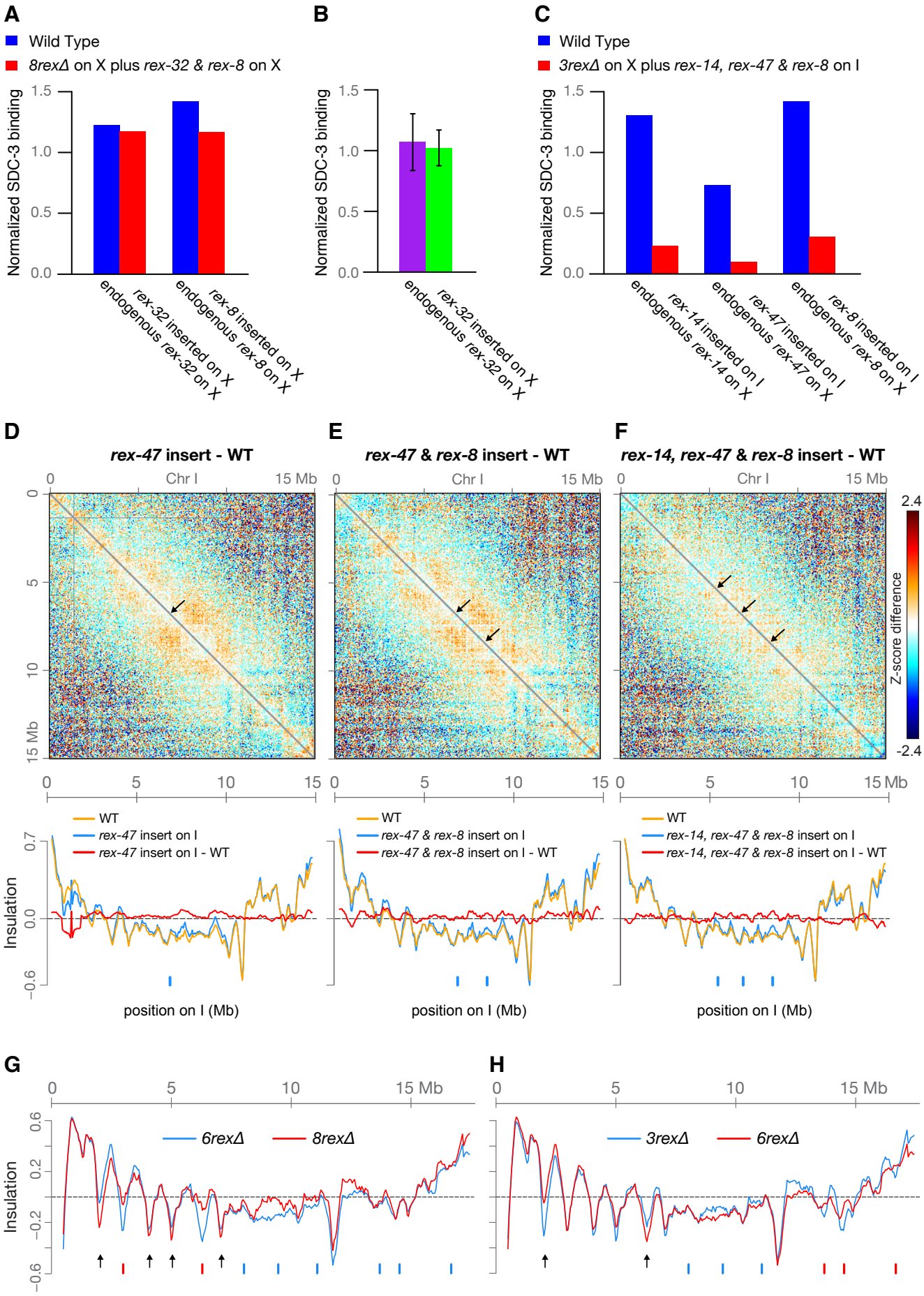
A
Wild Type
8rexΔ on X plus rex-32 & rex-8 on X
Normalized SDC-3 binding
1.5
1.0
0.5
0.0
endogenous rex-32 on X
rex-32 inserted on X
endogenous rex-8 on X
rex-8 inserted on X
B
Normalized SDC-3 binding
endogenous rex-32 on X
rex-32 inserted on X
C
Wild Type
3rexΔ on X plus rex-14, rex-47 & rex-8 on I
Normalized SDC-3 binding
endogenous rex-14 on X
rex-14 inserted on I
endogenous rex-47 on X
rex-47 inserted on I
endogenous rex-8 on X
rex-8 inserted on I
D
rex-47 insert - WT
E
rex-47 & rex-8 insert - WT
F
rex-14, rex-47 & rex-8 insert - WT
0
Chr I
15 Mb
5
10
2.4
Z-score difference
-2.4
WT
rex-47 insert on I
rex-47 insert on I - WT
rex-47 & rex-8 insert on I
rex-47 & rex-8 insert on I - WT
rex-14, rex-47 & rex-8 insert on I
rex-14, rex-47 & rex-8 insert on I - WT
Insulation
0.7
0.0
−0.6
position on I (Mb)
G
H
6rexΔ
8rexΔ
3rexΔ
0.6
0.2
−0.2

Figure S4. *rex* Sites Inserted on Chromosome I Weakly Recruit the DCC But Do Not Create TAD Boundaries, Related to Figure 2

(A) SDC-3 binding at *rex-32* and *rex-8* inserted at new locations on X is similar to binding at the endogenous sites. Binding at *rex-32* and *rex-8* was normalized to the average binding at four strong non-boundary *rex* sites within the same dataset (*rex-40*, *rex-23*, *rex-16*, and *Prex-30*). Binding was calculated by summing ChIP-seq reads mapping within 200 bp of the summit.

(B) SDC-3 binding at *rex-32* inserted at 15.5 Mb on the wild-type X chromosome is equivalent to binding at the endogenous *rex-32* site as measured by ChIP-qPCR. Binding was normalized to the binding at five strong *rex* sites (*rex-32*, *rex-8*, *rex-16*, *rex-48*, and *rex-35*). Error bars show standard deviation of three biological replicates.

(C) ChIP-seq experiments show that SDC-3 binding at three *rex* sites inserted on chromosome I is lower than binding at the endogenous sites on X. Binding was calculated and normalized as in (A).

(D-F) Z-score subtraction heatmaps binned at 50 kb show increased (red) and decreased (blue) Hi-C interactions in strains with one, two, or three *rex* sites inserted on chromosome I of the *3rexΔ* strain. This strain lacked the sites on X to allow unique mapping of reads to the new insertion locations. Arrows mark positions of inserted *rex* sites. *rex* insertions have no effect on chromosome I structure. Plots (below) show insulation scores across chromosome I in *rex* insertion (blue) and wild-type (orange) strains and the insulation score difference between genotypes (red). Chromosome I data used as the wild-type reference were from the strain carrying the *3rexΔ* X chromosome.

(G) Insulation profiles comparing X chromosomes in *6rexΔ* and *8rexΔ* strains. Blue ticks show *rex* sites deleted in both mutants, and red ticks show *rex* sites deleted only in the *8rexΔ* strain. Boundaries adjacent to the *rex* sites deleted only in the *8rexΔ* strain are strengthened (arrows).

(H) Insulation profiles comparing X chromosomes in *3rexΔ* and *6rexΔ* strains. Blue ticks show *rex* sites deleted in both mutants and red ticks show *rex* sites deleted only in *6rexΔ*. Insulation scores change at boundaries far from the deleted boundaries (arrows).

Figure S5

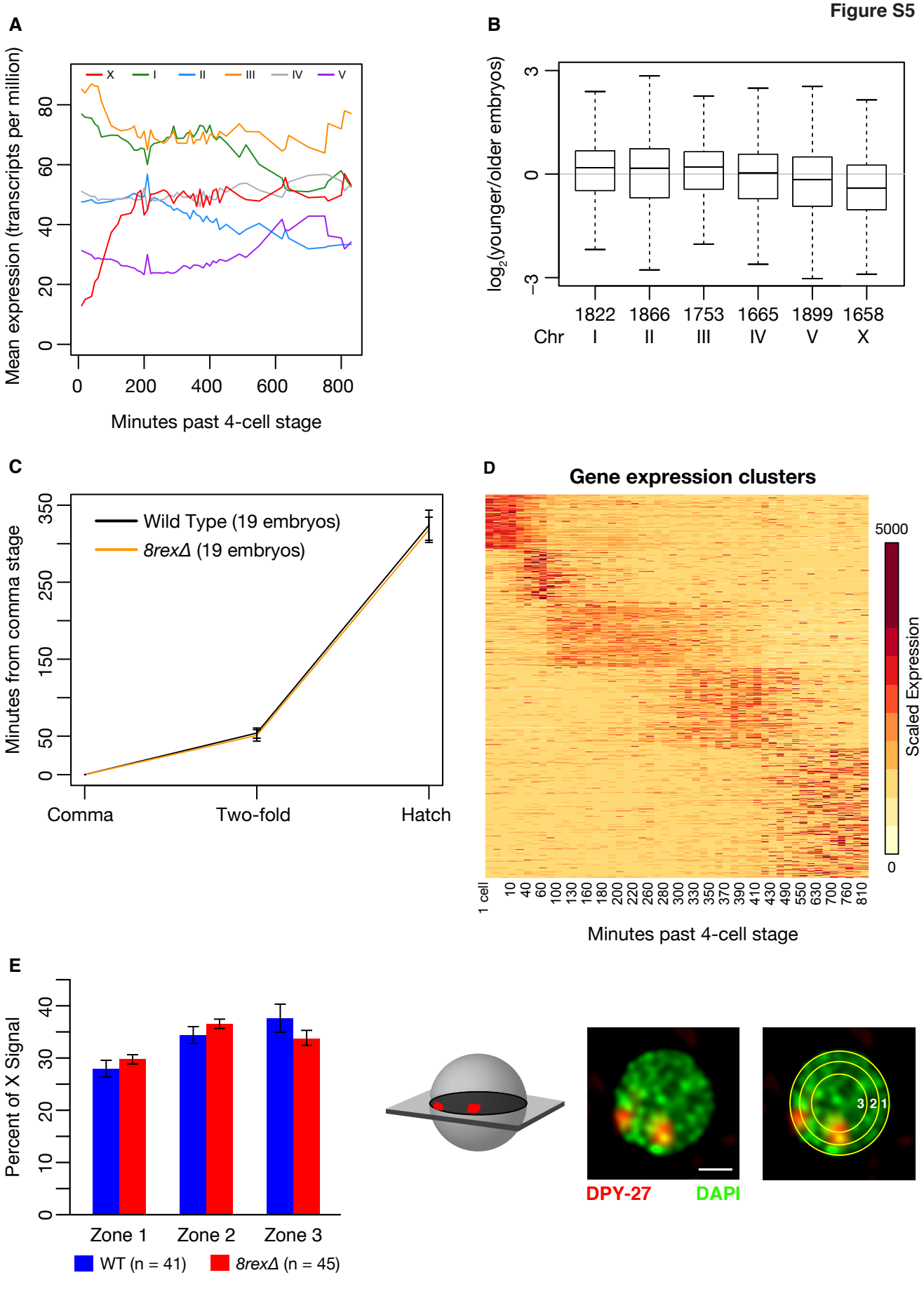
A
Mean expression (transcripts per million)
X
I
II
III
IV
V
0
20
40
60
80
0
200
400
600
800
Minutes past 4-cell stage
B
log2(younger/older embryos)
3
0
−3
1822
1866
1753
1665
1899
1658
Chr
I
II
III
IV
V
X
C
Minutes from comma stage
Wild Type (19 embryos)
8rexΔ (19 embryos)
0
50
150
250
350
Comma
Two-fold
Hatch
D
Gene expression clusters
5000
0
Scaled Expression
1 cell
10
40
60
100
130
160
180
200
220
260
280
300
330
350
370
390
410
430
490
550
630
700
760
810
Minutes past 4-cell stage
E
Percent of X Signal
0
10
20
30
40
Zone 1
Zone 2
Zone 3
WT (n = 41)
8rexΔ (n = 45)
3
2
1
DPY-27
DAPI

Figure S5. Analysis for Matching Age Distribution of Embryo Populations, Related to Figure 3

(A) Average expression from RNA-seq data (Hashimshony et al., 2015) of all the genes on each chromosome plotted at each time point during embryogenesis.

(B) Chromosome-by-chromosome comparison of gene expression in younger versus older wild-type embryos. Two replicates are included for each age. Because X chromosome silencing is gradually lost during early development, genes on X have lower expression in the younger population.

(C) The average time for development from comma stage to two-fold stage and then to hatching is equivalent in wild-type and *8rexΔ* embryos. Error bars show standard deviation.

(D) Expression for genes whose transcript levels change during development. Using data from (Hashimshony et al., 2015), we selected genes that have >1 transcript per million at any measured time point during embryogenesis and also change at least 20-fold in expression. We scaled each gene's expression by subtracting its mean and dividing by its standard deviation. The genes were divided into five groups by k-means clustering.

(E) X chromosome radial positioning is similar in nuclei of wild-type and *8rexΔ* embryos. (right) X chromosomes were stained with DPY-27 antibody (red) and DNA was stained with DAPI (green). For each nucleus, the Z section with the highest DPY-27 signal was selected. The nucleus was divided into three concentric zones of equal area, and the percentage of DPY-27 signal in each zone was calculated. (left) The graph shows the average percentage of X in each zone for wild-type and *8rexΔ* nuclei. Error bars show SEM. Scale bar is 1 μm.

Figure S6

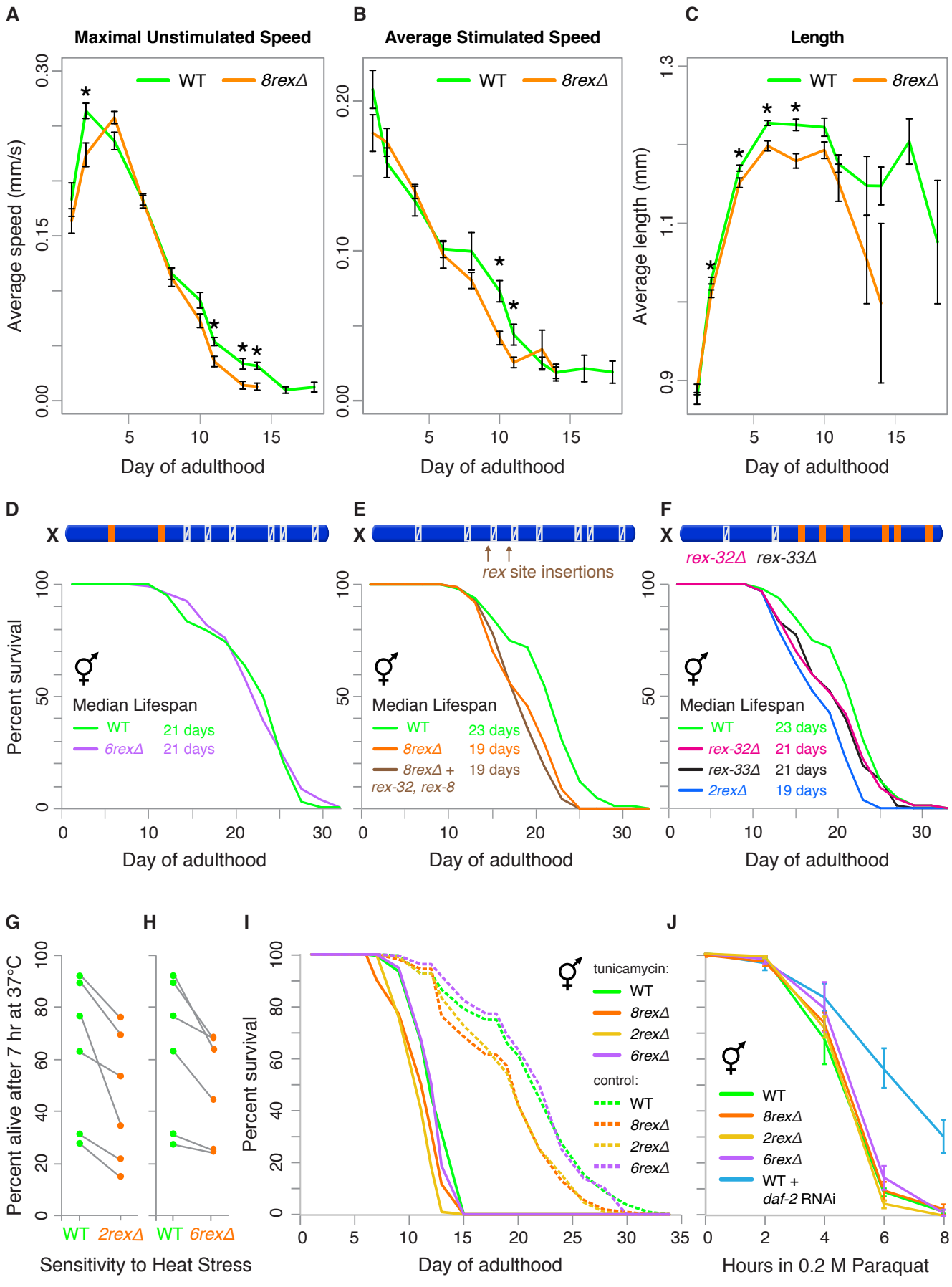
A
Maximal Unstimulated Speed
WT
8rexΔ
Average speed (mm/s)
Day of adulthood
B
Average Stimulated Speed
C
Length
Average length (mm)
D
X
Median Lifespan
WT 21 days
6rexΔ 21 days
Percent survival
E
rex site insertions
WT 23 days
8rexΔ 19 days
8rexΔ + rex-32, rex-8 19 days
F
rex-32Δ rex-33Δ
WT 23 days
rex-32Δ 21 days
rex-33Δ 21 days
2rexΔ 19 days
G
Percent alive after 7 hr at 37°C
WT 2rexΔ
H
WT 6rexΔ
Sensitivity to Heat Stress
I
tunicamycin:
WT
8rexΔ
2rexΔ
6rexΔ
control:
Day of adulthood
J
WT + daf-2 RNAi
Hours in 0.2 M Paraquat

Figure S6. Shortened Lifespan, Accelerated Aging, and Reduced Thermotolerance of Hermaphrodites with *rex* Deletions, Related to Figure 5

(A) Maximal unstimulated movement of wild-type and *8rexΔ* hermaphrodites during aging. For each genotype, the speed of 50 worms on each of eight plates was measured throughout adulthood. The measurement only included moving worms, not immobile or dead worms. We calculated the maximum speed of worms on each plate and plotted the mean ± SEM of eight plates. Asterisks indicate significant differences ($p < 0.05$, t test). mm/s, millimeters per second

(B) Average movement speed of wild-type and *8rexΔ* hermaphrodites in response to a mechanical stimulus (plate tap) during aging. Mean ± SEM of all eight plates are plotted as in (A).

(C) Body length of wild-type and *8rexΔ* hermaphrodites during aging. Mean ± SEM of all eight plates are plotted as in (A).

(D) Lifespans of wild-type versus *6rexΔ* hermaphrodites ($p = 0.8$, logrank test).

(E) Lifespans of wild-type versus *8rexΔ* hermaphrodites ($p < 0.0001$) or versus *8rexΔ* + *rex-32, rex-8* hermaphrodites ($p < 0.0001$).

(F) Lifespan of wild-type hermaphrodites versus *rex-32Δ* ($p = 0.06$) or versus *rex-33Δ* ($p = 0.03$) or versus *2rexΔ* ($p < 0.0001$). For (D-F), values from replicate experiments are presented in Table S6.

(G and H) Percent survival of wild-type and *2rexΔ* or *6rexΔ* day 1 adult worms after 7 hr at 37°C in each of six trials shows reduced thermotolerance in both *2rexΔ* and *6rexΔ* adults ($p= 0.0135$ and $p = 0.0183$, respectively, paired t test). Fifty worms of each genotype were counted in each trial. A gray line links the measurements of the two genotypes in the same trial. Replicate experiments and statistics are in Table S4.

(I) Lifespans were scored for wild-type, *8rexΔ*, *2rexΔ*, and *6rexΔ* hermaphrodites transferred on day 1 of adulthood to plates containing either 20 ng/μL tunicamycin to induce ER unfolded protein stress (solid lines) or DMSO as a control (dashed lines). Lifespans of all strains grown on tunicamycin were reduced. As in control experiments, lifespans of *8rexΔ* and *2rexΔ* adults grown on tunicamycin were shorter than those of wild-type and *6rexΔ* adults on tunicamcyin. The degree of lifespan reduction was similar across all genotypes, indicating similar sensitivity to ER unfolded protein stress. Replicate experiments and statistics are in Table S5.

(J) Percent survival of day 1 adult wild-type, *8rexΔ*, *2rexΔ*, and *6rexΔ* hermaphrodites in 0.2 M paraquat to induce reactive oxygen species in mitochondria. Wild-type worms subjected to *daf-2* RNAi were used as a control for increased oxidative stress tolerance. For each genotype, the average ± SEM of at least three replicates is plotted.

Table S1. Locations of *rex* site deletions and insertions, Related to Figure 1; Figure 2

***rex* site**	**Deletion location**	**Deletion size**	**Genomic location**	**Distance to nearest protein-coding gene**	**Cas9 guide RNA target sequence (protospacer)**
rex-32	X:2996734 to 2997626	892 bp	intergenic	677 bp *Y41G9A.6*	constructed using TALENs Lo et al., 2013
rex-33	X:6296494 to 6297792	1298 bp	genic	last intron of *mom-1* (Thorpe et al., 1997)	ccatttacatttggcgcagg and taacttattttacagaaaac
rex-14	X:8035969 to 8037090	1121 bp	intergenic	423 bp *xol-1*	atccacattactgtggttgg and cctttcacaacactcttttc
rex-47	X:9465542 to 9465960	418 bp	intergenic	817 bp *ZK899.6*	gtagtcacaccgaattgata Crane et al., 2015
rex-8	X:11093785 to 11094686	901 bp	intergenic	2395 bp *W02H3.3*	agttgaaacaccatggagcgg and gcaacttatcggtgtcgcgg
rex-43	X:13700642 to 13701123	481 bp	intergenic	4842 bp *adm-2*	ttggattgtgttcatcgtgg and aatgtcattaggttaaatg
rex-48	X:14525672 to 14526080	408 bp	intergenic	491 bp *nspc-17*	ccagcatttttgagtgctt
rex-35	X:16681790 to 16682252	462 bp	intergenic	1967 bp *F22H10.2*	ctatatacatgtttgaaac and tgttattctatttctaaag

***rex* site**	**Insertion location**	**Insertion size**	**Inserted sequence**	**Distance to nearest protein-coding gene**	**Cas9 guide RNA target sequence (protospacer)**
rex-32	X:7812122	592 bp	X:2996832 to 2997424	2988 bp *R03G5.6*	gtagaatgctccgtgtatgg
rex-8	X:9198531	754 bp	X:11093928 to 11094681	4149 bp *Y81B9A.1*	agtggactccatcacactgg
rex-14	I:5448650	500 bp	X:8036158 to 8036657	1795 bp *F27C1.13*	atttactgccaaacaggggg
rex-47	I:6858675	419 bp	X:9465601 to 9466019	1146 bp *glh-1*	ttccaaatcaggccgtaggg
rex-8	I:8507023	796 bp	X:11093891 to 11094686	2018 bp *sec-22*	cgtggtagtggtagaagcgg
rex-32	X:15574677	592 bp	X:2996832 to 2997424	984 bp *dyn-1*	ttatgtagtctctttcagtg

The genes nearest each deleted *rex* site do not show significant expression changes in *8rexΔ* compared to wild-type embryos (all q values > 0.99 and fold changes < 2).

Table S2. Statistics for Hi-C libraries, related to Figure 1; Figure 2; Figure S2; Figure S4.

Genotype	sequencing ID	Read pairs sequenced	Mapped paired-end reads	Hi-C contacts	cis contacts	% cis contacts	contacts ≤20kb	contacts >20kb	trans contacts
Wild type, replicate 1	BMEA008	345,019,879	282,509,400	165,106,057	108,180,356	65.5	18,537,295	89,643,061	56,925,701
Wild type, replicate 2	BMQB011	347,282,747	285,963,877	174,488,311	120,023,946	68.8	19,440,906	100,583,040	54,464,365
DCC mutant, replicate 1	BMEA014	343,219,970	282,454,019	212,570,004	162,743,891	76.6	28,524,650	134,219,241	49,826,113
DCC mutant, replicate 2	BMEA015	335,462,364	275,027,515	226,964,909	172,371,804	75.9	29,473,750	142,898,054	54,593,105
rex-47Δ, replicate 1	BMEA007	294,081,104	243,068,670	153,945,373	125,150,766	81.3	28,931,142	96,219,624	28,794,607
rex-47Δ, replicate 2	BMEA009	338,247,895	276,996,740	165,220,501	110,622,381	67.0	17,894,594	92,727,787	54,598,120
3rexΔ	BMEA027	318,171,138	258,390,604	148,851,059	118,655,892	79.7	27,718,268	90,937,624	30,195,167
6rexΔ, replicate 1	BMEA005	357,347,563	295,322,718	104,132,475	71,384,861	68.6	13,393,596	57,991,265	32,747,614
6rexΔ, replicate 2	BMEA010	346,012,880	283,577,018	156,033,638	107,310,063	68.8	19,405,386	87,904,677	48,723,575
8rexΔ, replicate 1	BMEA011	332,906,702	279,292,784	122,811,741	109,070,728	88.8	31,604,873	77,465,855	13,741,013
8rexΔ, replicate 2	BMEA012	321,206,155	263,925,332	174,496,009	138,646,425	79.5	37,428,958	101,217,467	35,849,584
8rexΔ plus *rex-32*	BMEA034	289,222,774	238,607,345	147,738,802	123,184,375	83.4	30,757,996	92,426,379	24,554,427
8rexΔ plus *rex-32* & *rex-8*	BMEA038	312,384,765	254,262,569	179,289,194	122,937,082	68.6	16,183,574	106,753,508	56,352,112
rex-32 insert	BMAS001	340,895,823	273,682,301	204,321,406	158,275,799	77.5	25,154,746	133,121,053	46,045,607
3rexΔ plus *rex-47* on I	BMEA028	291,839,702	236,564,530	132,176,851	107,531,507	81.4	25,669,424	81,862,083	24,645,344
3rexΔ plus *rex-47* & *rex-8* on I	BMEA029	330,676,073	279,160,255	132,500,704	110,416,797	83.3	26,804,337	83,612,460	22,083,907
3rexΔ plus *rex-14, rex-47* & *rex-8* on I	BMEA035	295,667,838	240,271,869	147,744,551	113,255,151	76.7	28,417,402	84,837,749	34,489,400

For each Hi-C experiment, the table gives the total number of paired end reads, the number of pairs for which both ends mapped, the number of valid Hi-C contacts after filtering (as in Brejc et al., 2017, Imakaev et al., 2012), and the number of contacts between pairs of loci on the same chromosome (within 20 kb or greater than 20 kb) and on different chromosomes.

Table S3. Wild-type and *8rexΔ* hermaphrodites have similar brood sizes and viability, Related to Figure 3

Genotype	Total embryos	Total adults	Broods counted	Viability	Average Brood Size	Brood Size Standard Deviation
Trial 1						
WT	2572	2593	10	1.01	257	37
8rexΔ	2256	2310	9	1.02	251	27
Trial 2						
WT		2798	9		311	53
8rexΔ		2685	9		298	36
Trial 3						
WT		2980	9		331	29
8rexΔ		3115	10		312	29

Wild-type and *8rexΔ* brood sizes are not significantly different (Trial 1 p = 0.87, Trial 2 p = 0.56, Trial 3 p = 0.16, two-tailed t test).

Table S4. *8rexΔ, 2rexΔ, and 6rexΔ* have significantly lower thermotolerance than wild-type adults, Related to Figure 5

	Percent alive after 37°C heat stress			
Trial (hours at 37°C)	**WT**	***8rexΔ***	***2rexΔ***	***6rexΔ***
Trial 1 (5 hr)	82%	68%		
Trial 2 (7 hr)	74%	46%		
Trial 3 (7 hr)	49%	30%		
Trial 4 (7 hr)	88%	54%		
Trial 5 (7 hr)	53%	37%		
Trial 6 (7 hr)	43%	34%		
Trial 7 (6 hr)	83%	76%	68%	57%
Trial 8 (6 hr)	38%	28%	36%	31%
Trial 9 (7 hr)	27%	30%	14%	24%
Trial 10 (7 hr)	31%	30%	21%	25%
Trial 11 (7 hr)	89%	80%	69%	68%
Trial 12 (7 hr)	76%	31%	34%	68%
Trial 13 (7 hr)	63%	40%	53%	44%
Trial 14 (7 hr)	92%	62%	76%	63%
Trial 15 (9.5 hr)	70%	34%	63%	33%
p value compared to WT (all Trials)	-	0.0001	0.0043	0.0024
p value compared to *8rexΔ* (all Trials)	0.0001	-	0.6175	0.9671
p value compared to *2rexΔ* (all Trials)	0.0043	0.6175	-	0.7036
p value compared to WT (7 hr Trials)	-	0.0014	0.0135	0.0183
p value compared to *8rexΔ* (7 hr Trials)	0.0014	-	0.8564	0.6761
p value compared to *2rexΔ* (7 hr Trials)	0.0135	0.8564	-	0.571

Sensitivity to heat stress was assessed by counting the percentage of day 1 adults that survive at 37°C for the indicated number of hours. P values were calculated using a two-tailed paired t test. WT, wild type

Table S5. Wild-type, *8rexΔ, 2rexΔ,* and *6rexΔ* hermaphrodites have similar tunicamycin sensitivity, Related to Figure 5

Genotype	Median Lifespan (Days)	Worms counted	Total Worms	P value compared to WT with tunicamycin	P value compared to *8rexΔ* with tunicamycin	P value compared to WT without tunicamycin
Trial 1						
WT	19	96	120	< 0.0001	< 0.0001	
8rexΔ	17	94	120	< 0.0001	< 0.0001	0.0004
WT tunicamycin	13	98	120		0.2939	< 0.0001
8rexΔ tunicamycin	12	102	120	0.2939		< 0.0001
Trial 2						
WT	24	92	120	< 0.0001	0.3192	
8rexΔ	20	84	120	0.3192	< 0.0001	< 0.0001
WT tunicamycin	19	110	120		< 0.0001	< 0.0001
8rexΔ tunicamycin	19	105	120	< 0.0001		< 0.0001
Trial 3						
WT tunicamycin	12	103	120		0.0002	< 0.0001
8rexΔ tunicamycin	12	106	120	0.0002		< 0.0001
2rexΔ tunicamycin	11	109	120	< 0.0001	0.0188	< 0.0001
6rexΔ tunicamycin	12	109	120	0.338	0.002	< 0.0001
WT	22	100	120	< 0.0001	< 0.0001	
8rexΔ	20	97	120	< 0.0001	< 0.0001	0.0018
2rexΔ	20	104	120	< 0.0001	< 0.0001	0.001
6rexΔ	22	99	120	< 0.0001	< 0.0001	0.9858
Trial 4						
WT tunicamycin	12	101	120		0.0084	< 0.0001
8rexΔ tunicamycin	11	94	120	0.0084		< 0.0001
2rexΔ tunicamycin	12	100	120	0.3653	0.0605	< 0.0001
6rexΔ tunicamycin	12	98	120	0.0086	< 0.0001	< 0.0001
WT	18	101	120	< 0.0001	< 0.0001	
8rexΔ	16	94	120	< 0.0001	< 0.0001	< 0.0001
2rexΔ	16	100	120	< 0.0001	< 0.0001	< 0.0001
6rexΔ	18	98	120	< 0.0001	< 0.0001	0.1227

Sensitivity to ER unfolded protein stress was assessed by measuring hermaphrodite lifespan on plates containing 20 ng/µl tunicamycin, which causes accumulation of unfolded glycoproteins in the ER. “Worms counted” is the number of worm deaths tallied. “Total worms” is the initial number of worms, including those that were censored from the experiment because they crawled off the plate. P values were calculated using the logrank test. Tunicamycin exposure reduced the lifespan of all genotypes. As in control experiments, lifespans of *8rexΔ* and *2rexΔ* adults on tunicamycin were shorter than those of wild-type and *6rexΔ* adults on tunicamcyin. The degree of lifespan reduction was similar across all genotypes, indicating similar sensitivity to ER unfolded protein stress. WT, wild type.

Table S6. Statistics for hermaphrodite and male lifespan experiments, Related to Figure 5

Genotype	Median Lifespan (Days)	Worms counted	Total Worms	P value compared to WT	P value compared to *8rexΔ*
Hermaphrodite Trial 1					
WT	21	77	108		
8rexΔ	17	90	120	< 0.0001	
Hermaphrodite Trial 2					
WT	23	89	120		
8rexΔ	19	102	120	< 0.0001	
rex-32Δ rex-33Δ	19	88	120	< 0.0001	
rex-32Δ	21	98	120	0.055	0.0226
rex-33Δ	21	100	120	0.0304	0.0196
8rexΔ plus rex-32 & rex-8	19	103	120	< 0.0001	0.02218
Hermaphrodite Trial 3					
WT	21	78	120		
8rexΔ	17	100	120	< 0.0001	
6rexΔ	21	92	120	0.7959	< 0.0001
rex-32Δ rex-33Δ	17	109	120	< 0.0001	0.0632
Hermaphrodite Trial 4					
WT	20	92	120		
6rexΔ	18	88	120	0.1974	
rex-32Δ	18	78	120	0.189	
rex-33Δ	20	93	120	0.5062	
Male Trial 1					
WT males	14	169	300		
8rexΔ males	14	133	300	0.2485	
Male Trial 2					
WT males	18	146	310		
8rexΔ males	16	89	300	0.0633	

“Worms counted” is the number of worm deaths tallied. “Total worms” is the initial number of worms, including those that were censored from the experiment because they crawled off the plate. As observed previously, the majority of males crawled off the plate before dying. P values were calculated using the logrank test. WT, wild type